

1 **Rheologic constraints on the upper mantle from five years of**
2 **postseismic deformation following the El Mayor-Cucapah**
3 **earthquake**

4 **T. T. Hines¹, E. A. Hetland¹**

5 ¹Department of Earth and Environmental Sciences, University of Michigan, Ann Arbor, Michigan, USA.

6 **Key Points:**

- 7 • Transient postseismic deformation can be observed following the El Mayor-Cucapah
8 earthquake at epicentral distances of up to 400 km
9 • Near-field postseismic deformation exhibits early transience that decays to a sustained
10 rate which is elevated above the preseismic trend
11 • Far-field postseismic deformation can be explained with a Zener or Burgers rheology
12 upper mantle

13 **Abstract**

14 We analyze five years of Southern California GPS data following the Mw=7.2 El Mayor-Cucapah
 15 earthquake. We observed transient postseismic deformation which persists for three years at
 16 epicentral distances greater than ~ 200 km. In the near-field, rapid postseismic transience de-
 17 cays to a sustained rate which exceeds its preseismic trend. We attempt to determine the mech-
 18 anisms driving this deformation, where we consider afterslip at seismogenic depths and vis-
 19 coelastic relaxation in the lower crust and upper mantle as candidate mechanisms. We find that
 20 early, rapid, near-field deformation can be explained with afterslip on the fault that ruptured
 21 coseismically. The later, sustained, near-field deformation can be explained with either con-
 22 tinued afterslip in an effectively elastic lower crust, or lower crustal viscoelastic relaxation with
 23 a steady-state viscosity of $\sim 10^{19}$ Pa s. The later postseismic deformation in the far-field is best
 24 explained with a transient viscosity of $\sim 10^{18}$ Pa s in the upper mantle. We argue that a tran-
 25 sient rheology in the mantle is preferable over a Maxwell rheology because it better predicts
 26 the decay in postseismic deformation, and also because it does not conflict with the generally
 27 higher, steady-state viscosities inferred from studies of geophysical processes occurring over
 28 longer time-scales.

29 **1 Introduction**

30 Ground deformation in the years following a large ($Mw \gtrsim 7$) earthquake can be used to
 31 gain insight into the mechanical behavior of the crust and upper mantle. The interpretations
 32 of postseismic deformation are not always conclusive because multiple postseismic deforma-
 33 tion mechanisms, such as afterslip or viscoelastic relaxation in the lower crust and upper man-
 34 tle, can have qualitatively similar surface expressions [e.g. Savage, 1990]. This non-uniqueness
 35 complication can potentially be remedied if the postseismic deformation occurs in an area that
 36 is sufficiently well instrumented with GPS stations [Hearn, 2003]. Owing to the dense geode-
 37 metic network deployed throughout the 2000s as part of the Plate Boundary Observatory, the post-
 38 seismic deformation following the April 4, 2010, Mw=7.2 El Mayor-Cucapah earthquake in
 39 Baja California was observed at more GPS stations than any other earthquake in California
 40 to date (see Hauksson *et al.* [2011] and Fletcher *et al.* [2014] for a detailed description of this
 41 earthquake and its seismotectonic context). With such a large collection of data, we attempt
 42 to discern the mechanisms driving the postseismic deformation.

43 Previous studies which have modeled postseismic deformation following the El Mayor-
 44 Cucapah earthquake include Pollitz *et al.* [2012], Gonzalez-Ortega *et al.* [2014], Spinler *et al.*
 45 [2015], and Rollins *et al.* [2015]. Of these studies, Gonzalez-Ortega *et al.* [2014] and Rollins
 46 *et al.* [2015] have attempted to describe the postseismic deformation with afterslip in an elas-
 47 tic half-space. Gonzalez-Ortega *et al.* [2014] described five months of postseismic deforma-
 48 tion, observed by InSAR and GPS stations within ~ 50 km of the rupture, with afterslip and
 49 contraction on the coseismically ruptured fault. Gonzalez-Ortega *et al.* [2014] noted that their
 50 preferred model underestimated the GPS displacements for stations $\gtrsim 25$ km from the rup-
 51 ture and suggested that it could be the result of unmodeled viscoelastic relaxation. Using only
 52 continuous GPS stations, which are mostly north of the rupture zone, Rollins *et al.* [2015] found
 53 that three years of postseismic deformation can be adequately explained by afterslip, albeit with
 54 an implausibly large amount of slip inferred on the least constrained, southern-most fault seg-
 55 ment. Here, we suggest the afterslip inferred by Rollins *et al.* [2015] may have been acting as
 56 a proxy for distributed relaxation in the upper mantle.

57 Pollitz *et al.* [2012], Rollins *et al.* [2015] and Spinler *et al.* [2015] explored viscoelastic
 58 relaxation in the lower crust and upper mantle as a potential postseismic deformation mech-
 59 anism. The rheology of the crust and mantle is largely unknown and so modeling postseis-
 60 mic deformation with viscoelastic relaxation requires one to assume a rheologic model and
 61 then find the best fitting rheologic parameters. The inference of these rheologic parameters is
 62 a computationally expensive non-linear inverse problem which is typically approached with
 63 a forward modeling grid search method. Consequently, a simplified structure for the Earth must

be assumed in order to minimize the number of rheologic parameters that need to be estimated. For example, it is commonly assumed that the lower crust and upper mantle are homogeneous, Maxwell viscoelastic layers, which may be too simplistic for postseismic studies [Riva and Govers, 2009; Hines and Hetland, 2013]. To further reduce the dimensions of the model space, it is also necessary to make simplifying assumptions about the behavior of afterslip. For example, one can assume a frictional model for afterslip and parametrize afterslip in terms of the unknown rheologic properties of the fault [e.g. Johnson *et al.*, 2009; Johnson and Segall, 2004]. One can also assume that afterslip does not persist for more than a few months and then model the later postseismic deformation assuming it to be the result of only viscoelastic relaxation [e.g. Pollitz *et al.*, 2012; Spinler *et al.*, 2015]. However, afterslip in similar tectonic settings has been observed to persist for decades following earthquakes [Cakir *et al.*, 2012; Cetin *et al.*, 2014]. Indeed, the preferred viscoelastic model from Pollitz *et al.* [2012] significantly underestimates deformation in the Imperial Valley, which could be indicative of unmodeled continued afterslip. Neglecting to allow for sustained afterslip as a postseismic mechanism could then lead to biased inferences of viscosities.

In this study, we perform a kinematic inversion for fault slip, allowing it to persist throughout the postseismic period, while simultaneously estimating the viscosity of the lower crust and upper mantle. We create an initial model of the fault slip and effective viscosity necessary to describe early postseismic deformation using the method described in Hines and Hetland [2016]. This method uses a first-order approximation of surface deformation resulting from viscoelastic relaxation which is only applicable to the early postseismic period. In this case, our initial model describes the first 0.8 years of postseismic deformation following the El Mayor-Cucapah earthquake. We then use the inferred effective viscosity structure from the initial model to create a suite of postseismic models which we test against the five years of postseismic data available to date. Of the suite of models tested, we find that postseismic deformation following the El Mayor-Cucapah earthquake can be explained with a combination of afterslip on a fault segment running through the Sierra Cucapah and viscoelastic relaxation in a Zener rheology upper mantle with a transient viscosity on the order of 10^{18} Pa s.

2 Data Processing

We use continuous GPS position time series provided by University Navstar Consortium (UNAVCO) for stations within a 400 km radius about the El Mayor-Cucapah epicenter. We collectively describe the coseismic and postseismic displacements resulting from the El Mayor-Cucapah earthquake as $u_{\text{post}}(t)$. We consider the GPS position time series, $u_{\text{obs}}(t)$, to be the combination of $u_{\text{post}}(t)$, secular tectonic deformation, annual and semi-annual oscillations, and coseismic offsets from significant earthquakes over the time span of this study. The June 14, 2010, Mw=5.8 Ocotillo earthquake and the Brawley swarm, which included an Mw=5.5 and an Mw=5.4 event on August 26, 2012 (Figure 1), are the only earthquakes that produced noticeable displacements in any of the time series. We treat the displacements resulting from the Brawley swarm as a single event because the daily solutions provided by UNAVCO cannot resolve the separate events. Although the Ocotillo earthquake had its own series of aftershocks [Hauksson *et al.*, 2011], neither the Ocotillo earthquake nor the Brawley swarm produced detectable postseismic deformation. We model displacements resulting from these events with only a Heaviside function, $H(t)$, describing the coseismic offsets. We then model $u_{\text{obs}}(t)$ as

$$u_{\text{obs}}(t) = u_{\text{pred}}(t) + \epsilon, \quad (1)$$

where

$$\begin{aligned} u_{\text{pred}}(t) = & u_{\text{post}}(t)H(t - t_{\text{emc}}) + c_0 + c_1 t + \\ & c_2 \sin(2\pi t) + c_3 \cos(2\pi t) + c_4 \sin(4\pi t) + c_5 \cos(4\pi t) + \\ & c_6 H(t - t_{\text{oc}}) + c_7 H(t - t_{\text{bs}}). \end{aligned} \quad (2)$$

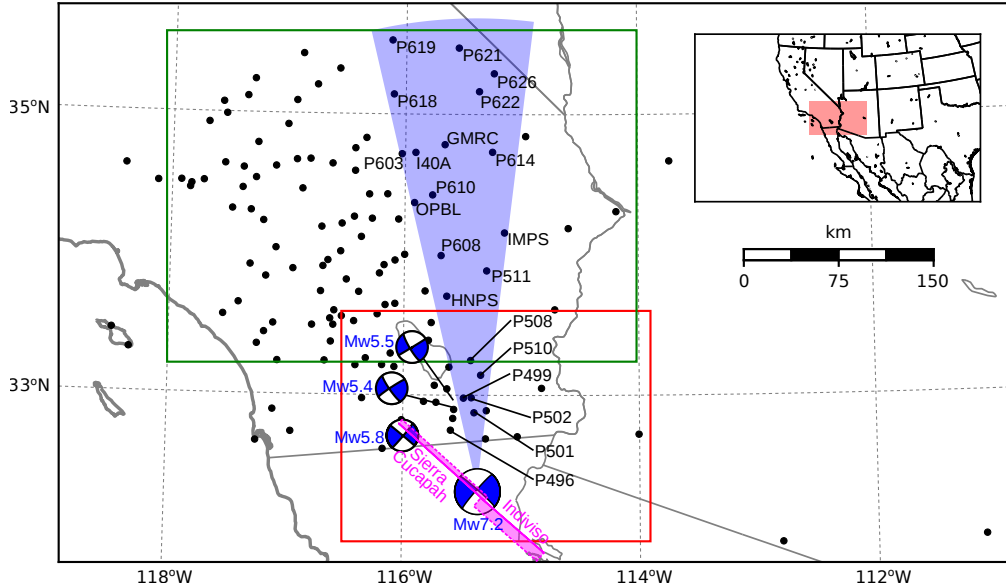


Figure 1. Map of the region considered in this study. The large focal mechanism is the GCMT solution for the El Mayor-Cucapah earthquake, and the three small focal mechanisms are for the Ocotillo earthquake and the two main shocks during the Brawley swarm. The black dots indicate the locations of GPS stations used in this study. The fault geometry used in this study is shown in magenta where dashed lines indicate buried edges of the fault segments. The green and red boxes demarcate the extent of the near-field and far-field maps (Figures 4 and 5). Stations inside the blue sector, which highlights the area within 10° of the El Mayor-Cucapah P-axis, are used in Figures 7 and 10.

In the above equations, t_{emc} , t_{oc} and t_{bs} are the times of the El Mayor-Cucapah earthquake, Ocotillo earthquake, and the Brawley swarm, respectively, c_0 through c_7 are unknown coefficients, and ϵ is the observation noise. We are using years as our unit of time which makes c_2 through c_5 the coefficients for annual and semi-annual oscillations. We only estimate jumps associated with the Ocotillo earthquake and Brawley swarm for stations within 40 km of their epicenters.

Stations which recorded displacements that clearly cannot be described by the aforementioned processes are not included in our analysis. This includes stations in the Los Angeles basin, where anthropogenic deformation can be larger than the postseismic signal that we are trying to estimate [Bawden *et al.*, 2001; Argus *et al.*, 2005]. In order to ensure an accurate estimation of the secular deformation, we only use stations that were installed at least six months prior to El Mayor-Cucapah earthquake even though several GPS stations were installed after the earthquake to get better coverage of the postseismic deformation field [Spiner *et al.*, 2015]. It would be possible to subtract secular velocities derived from elastic block models [e.g. Meade and Hager, 2005] from velocities recorded at the newly installed stations to get an estimate of postseismic velocities at those stations. However, estimating velocities from an already noisy displacement time series can introduce significant uncertainties depending on exactly how the estimation is done. We therefore use coseismic and postseismic displacements, rather than velocities, in our inverse method described in Section 3. This choice prevents us from using the newly installed stations for our analysis.

The October 16, 1999, Mw=7.1 Hector Mine earthquake, which occurred \sim 270 km north of the El Mayor-Cucapah epicenter, produced transient postseismic deformation which we do not wish to model, either mechanically or through empirical line fitting. We thus restrict our analysis to deformation observed six years after the Hector Mine earthquake, which is when

139 postseismic velocities at sites near the Hector Mine epicenter are approximately constant [Savage
 140 and Svare, 2009]. When appraising our model fit in Section 3, we see some systematic
 141 residuals in the vicinity of the Hector Mine epicenter, which may be the result of errors in the
 142 assumption that the trend in Hector Mine postseismic deformation is linear after six years.

143 Studies of postseismic deformation typically assume a parametric form for $u_{\text{post}}(t)$, such
 144 as one with a logarithmic or exponential time dependence [e.g. Savage *et al.*, 2005]. However,
 145 by assuming a logarithmic or exponential form of $u_{\text{post}}(t)$ we run the risk of over fitting the
 146 GPS time series and inferring a non-existent postseismic signal. We therefore do not assume
 147 any parametric form for $u_{\text{post}}(t)$ and rather treat it as integrated Brownian motion, so that

$$\dot{u}_{\text{post}}(t) = \sigma^2 \int_0^t w(s)ds, \quad (3)$$

148 where $w(t)$ is white noise and the variance of $\dot{u}_{\text{post}}(t)$ increases linearly with time by a factor
 149 of σ^2 . We use a Kalman filtering approach to estimate $u_{\text{post}}(t)$ and the unknown parameters
 150 in eq. (2). In the context of Kalman filtering, our time varying state vector is

$$\mathbf{X}(t) = [u_{\text{post}}(t), \dot{u}_{\text{post}}(t), c_0, \dots, c_7] \quad (4)$$

151 and eq. (2) is the observation function which maps the state vector to the GPS observations.
 152 We initiate the Kalman filter by assuming a prior estimate of $\mathbf{X}(t)$ at the first time epoch, denoted
 153 $\mathbf{X}_{1|0}$, which has a sufficiently large covariance, denoted $\Sigma_{1|0}$, to effectively make our
 154 prior uninformed. For each time epoch, t_i , Bayesian linear regression is used to incorporate
 155 GPS derived estimates of displacement with our prior estimate of the state, $\mathbf{X}_{i|i-1}$, to form
 156 a posterior estimate of the state, $\mathbf{X}_{i|i}$, which has covariance $\Sigma_{i|i}$. We then use the posterior
 157 estimate of the state at time t_i to form a prior estimate of the state at time t_{i+1} through the
 158 transition function

$$\mathbf{X}_{i+1|i} = \mathbf{F}_{i+1} \mathbf{X}_{i|i} + \delta_{i+1}, \quad (5)$$

159 where

$$\mathbf{F}_{i+1} = \begin{bmatrix} 1 & (t_{i+1} - t_i) & \mathbf{0} \\ 0 & 1 & \mathbf{0} \\ \mathbf{0} & \mathbf{0} & \mathbf{I} \end{bmatrix} \quad (6)$$

160 and δ_{i+1} is the process noise, which has zero mean and covariance described by

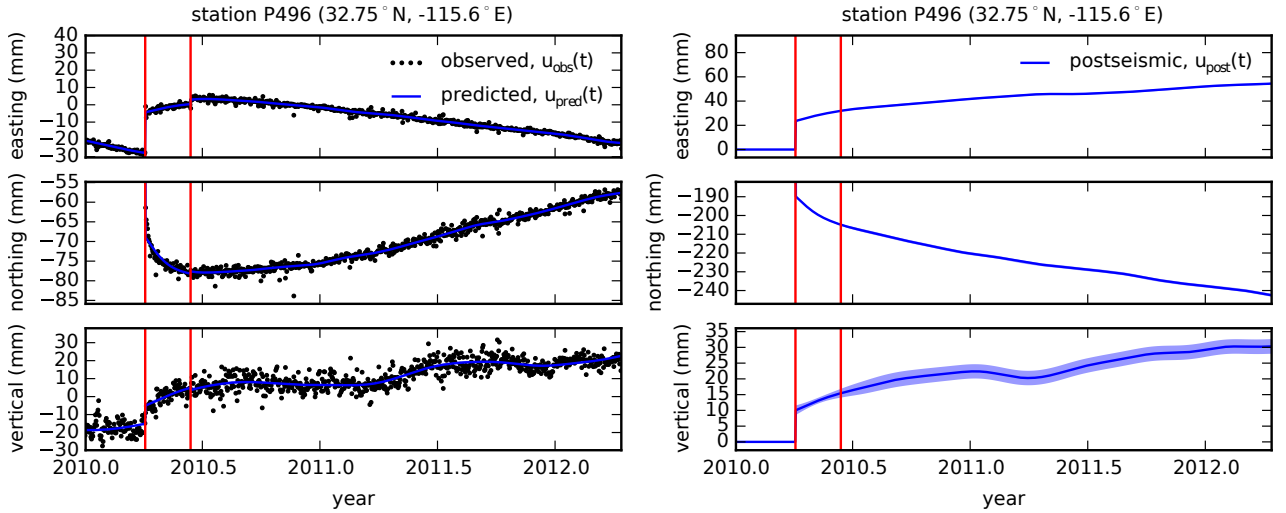
$$\mathbf{Q}_{i+1} = \sigma^2 \begin{bmatrix} \frac{(t_{i+1} - t_i)^3}{3} & \frac{(t_{i+1} - t_i)^2}{2} & \mathbf{0} \\ \frac{(t_{i+1} - t_i)^2}{2} & (t_{i+1} - t_i) & \mathbf{0} \\ \mathbf{0} & \mathbf{0} & \mathbf{0} \end{bmatrix}. \quad (7)$$

161 The covariance of the new prior state, $\mathbf{X}_{i+1|i}$, is then described by

$$\Sigma_{i+1|i} = \mathbf{F}_{i+1} \Sigma_{i|i} \mathbf{F}_{i+1}^T + \mathbf{Q}_{i+1}. \quad (8)$$

162 This process is repeated for each of the N time epochs. We then use Rauch-Tung-Striebel smoothing
 163 [Rauch *et al.*, 1965] to find $\mathbf{X}_{i|N}$, which is an estimate of the state at time t_i that incor-
 164 porates GPS observation for all N time epochs. Our final estimates of $u_{\text{post}}(t)$ are used in sub-
 165 sequent analysis, while the remaining components of the state vector are considered nuisance
 166 parameters. In the interests of computational tractability, we down sample our smoothed time
 167 series from daily solutions down to weekly solutions.

168 The smoothness of $u_{\text{post}}(t)$ is controlled by the chosen value of σ^2 , which describes how
 169 rapidly we expect postseismic displacements to vary over time. Setting σ^2 equal to zero will

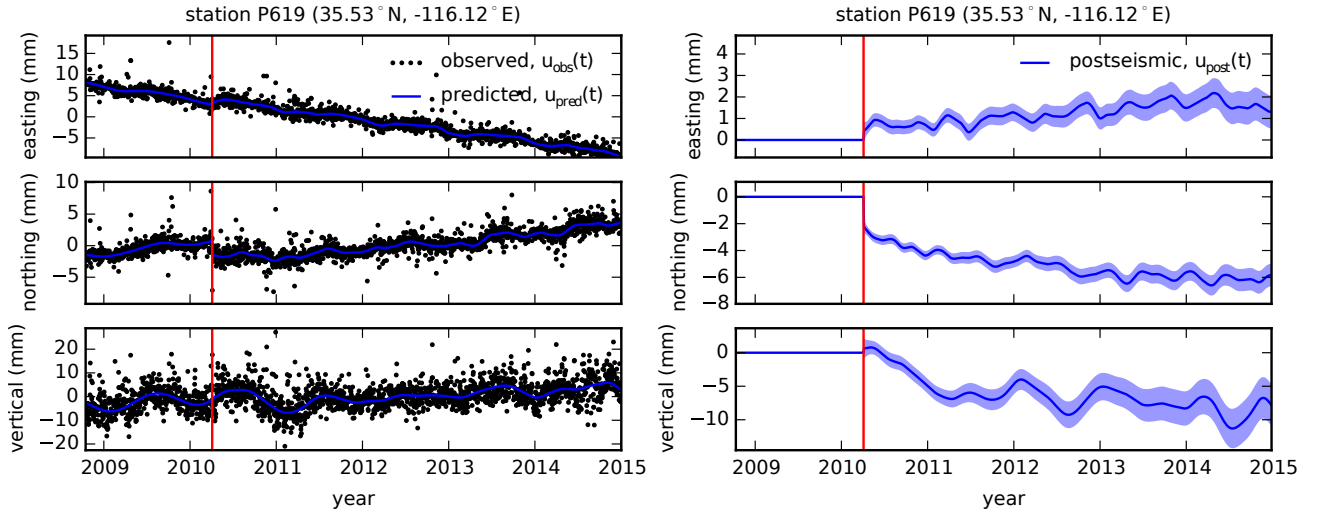


186 **Figure 2.** Left panels show GPS time series from UNAVCO (black) and the predicted displacement (blue)
 187 from eq. (2) for a near-field station. Red lines indicate the times of the El Mayor-Cucapah and Ocotillo earth-
 188 quake. The right panels show estimated coseismic and postseismic displacements, u_{post} , which are extracted
 189 from the predicted displacements. The 68% confidence interval is shown in light blue.

170 effectively result in modeling $u_{\text{post}}(t)$ as a straight line which is insufficient to describe the
 171 expected transient behavior in postseismic deformation. The other end member, where σ^2 is
 172 infinitely large, will result in $u_{\text{pred}}(t)$ overfitting the data. While one can use a maximum like-
 173 lihood based approach for picking σ^2 [e.g. Segall and Mathews, 1997], we instead take a sub-
 174 jective approach and choose a value for σ^2 that is just large enough to faithfully describe the
 175 observed deformation at the most near-field station in our study, P496, which exhibits the most
 176 rapid changes in velocity. This ensures that σ^2 will be sufficiently large so that our estimate
 177 of $u_{\text{post}}(t)$ does not smooth out potentially valuable postseismic signal at the remaining sta-
 178 tions. We find that using $\sigma^2 = 0.05 \text{ m}^2/\text{yr}^3$ adequately describes all but the first week of post-
 179 seismic deformation at station P496, which slightly increases our estimate of coseismic dis-
 180 placements (Figure 2). We include an example of estimating $u_{\text{post}}(t)$ for a far-field station,
 181 P619, which is about 359 km north of the El Mayor-Cucapah epicenter (Figure 3). At station
 182 P619, along with all the other stations in the Mojave region, there is a south-trending post-
 183 seismic transience that persists for the first three years after the El Mayor-Cucapah earthquake.
 184 Postseismic deformation that extends to these epicentral distances has also been observed af-
 185 ter the Hector Mine earthquake [Freed et al., 2007].

191 It is important to note that the shown uncertainties in $u_{\text{post}}(t)$ do not account for the non-
 192 negligible epistemic uncertainty in eq. (2). For example, we assume a constant rate of secu-
 193 lar deformation, which appears to be an appropriate approximation for all but perhaps the sta-
 194 tions closest to the Hector Mine epicenter, as noted above. Also, our model for seasonal de-
 195 formation in eq. (2) assumes a constant amplitude over time, which means that any yearly vari-
 196 ability in the climatic conditions could introduce systematic residuals [Davis et al., 2012]. In-
 197 deed, it would be more appropriate to consider the seasonal amplitudes $c_2 - c_5$ in eq. (2) as
 198 stochastic variables [Murray and Segall, 2005]. By using constant seasonal amplitudes, our es-
 199 timate of $u_{\text{post}}(t)$ seems to describe some of the unmodeled annual and semi-annual oscilla-
 200 tions (e.g. Figure 3).

201 We show in Figures 4 and 5 the near and far-field coseismic displacements and the post-
 202 seismic displacements accumulated over the time intervals 0–1 years, 1–3 years, and 3–5 years.
 203 Stations at epicentral distances beyond ~ 200 km have an elevated rate of deformation for the
 204 first three years following the earthquake. This far-field deformation is trending southward at



190 **Figure 3.** same as Figure 2 but for a far-field station.

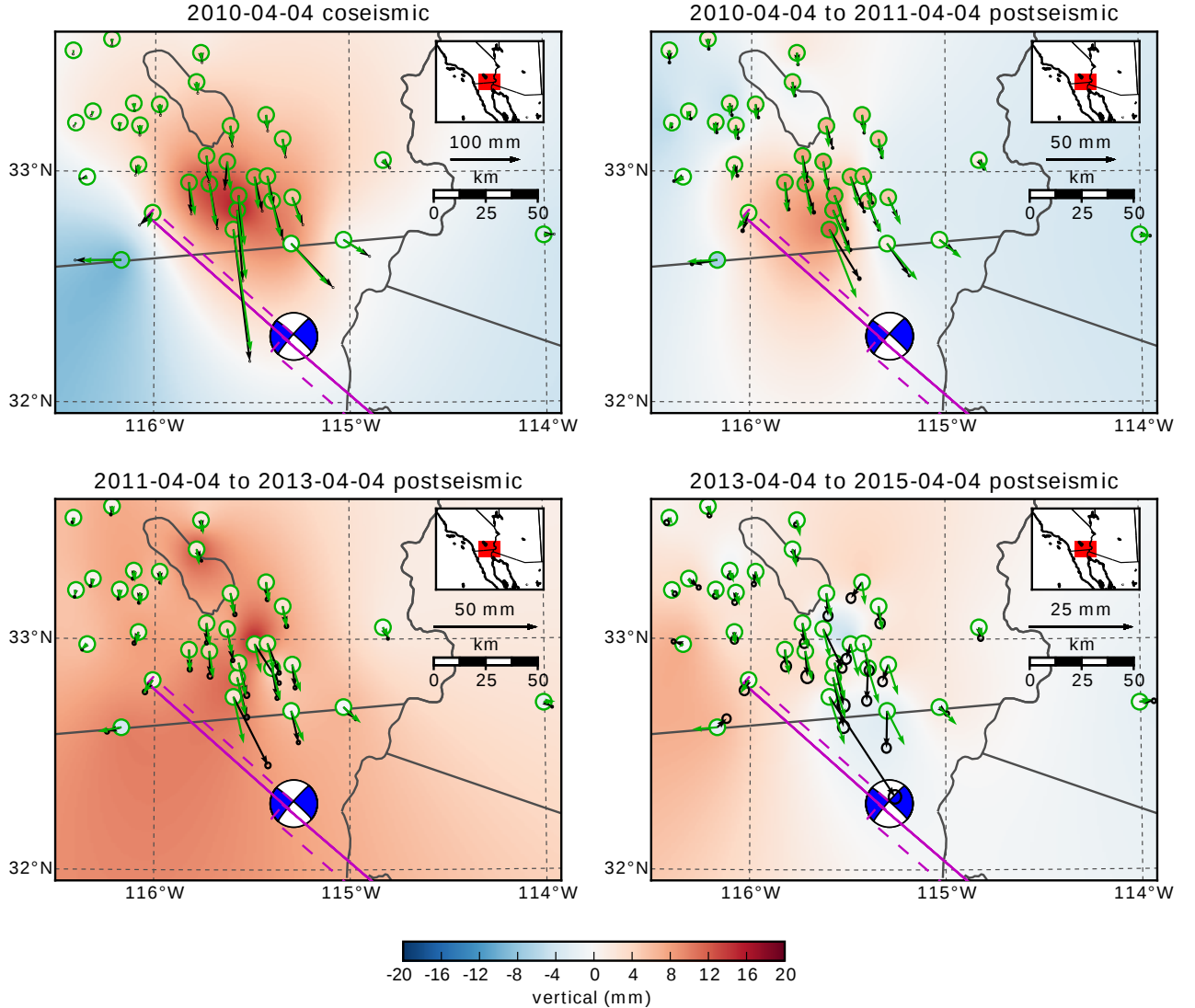
205 a rate of a few millimeters per year along the direction of the El Mayor-Cucapah P-axis. A
 206 similar eastward trend can be seen in the few far-field stations in Arizona, located along the
 207 T-axis. After three years, the trend in far-field postseismic deformation is barely perceptible.
 208 Most far-field stations display an initial subsidence for the first year after the El Mayor-Cucapah
 209 earthquake followed by continued uplift. This trend in vertical deformation can be observed
 210 in all three of the quadrants where postseismic data is available, which means that the verti-
 211 cal deformation does not exhibit an anti-symmetric quadrant pattern, as would be expected for
 212 postseismic processes. Although we use vertical deformation in our analysis in Section 3, we
 213 do not put an emphasis on trying to describe the vertical deformation because it likely does
 214 not have postseismic origins.

221 The near-field postseismic deformation is notably sustained when compared to the far-
 222 field deformation. Namely, the station in this study which is closest to the El Mayor-Cucapah
 223 epicenter, P496, has a steady postseismic trend of ~ 1.5 cm/yr to the south after about one year.
 224 Vertical postseismic deformation in the near-field does display a quadrant pattern which is con-
 225 sistent with the coseismic vertical deformation, suggesting that it is resulting from postseis-
 226 mic processes. However, the vertical postseismic signal is only apparent for the first year af-
 227 ter the earthquake (Figure 4). As with the far-field deformation, there is a general trend of up-
 228 lift in the near-field after about one year.

229 **3 Postseismic Modeling**

233 We seek to find the mechanisms driving five years of postseismic deformation follow-
 234 ing the El Mayor-Cucapah earthquake and we consider afterslip and viscoelastic relaxation as
 235 candidate mechanisms. Poroelastic rebound has also been used to model postseismic defor-
 236 mation [e.g. Jónsson *et al.*, 2003]; however, Gonzalez-Ortega *et al.* [2014] found that poroe-
 237 lastic rebound is unlikely to be a significant contributor to postseismic deformation following
 238 the El Mayor-Cucapah earthquake. Furthermore, we consider stations which are sufficiently
 239 far away from the rupture that poroelastic rebound should be insignificant.

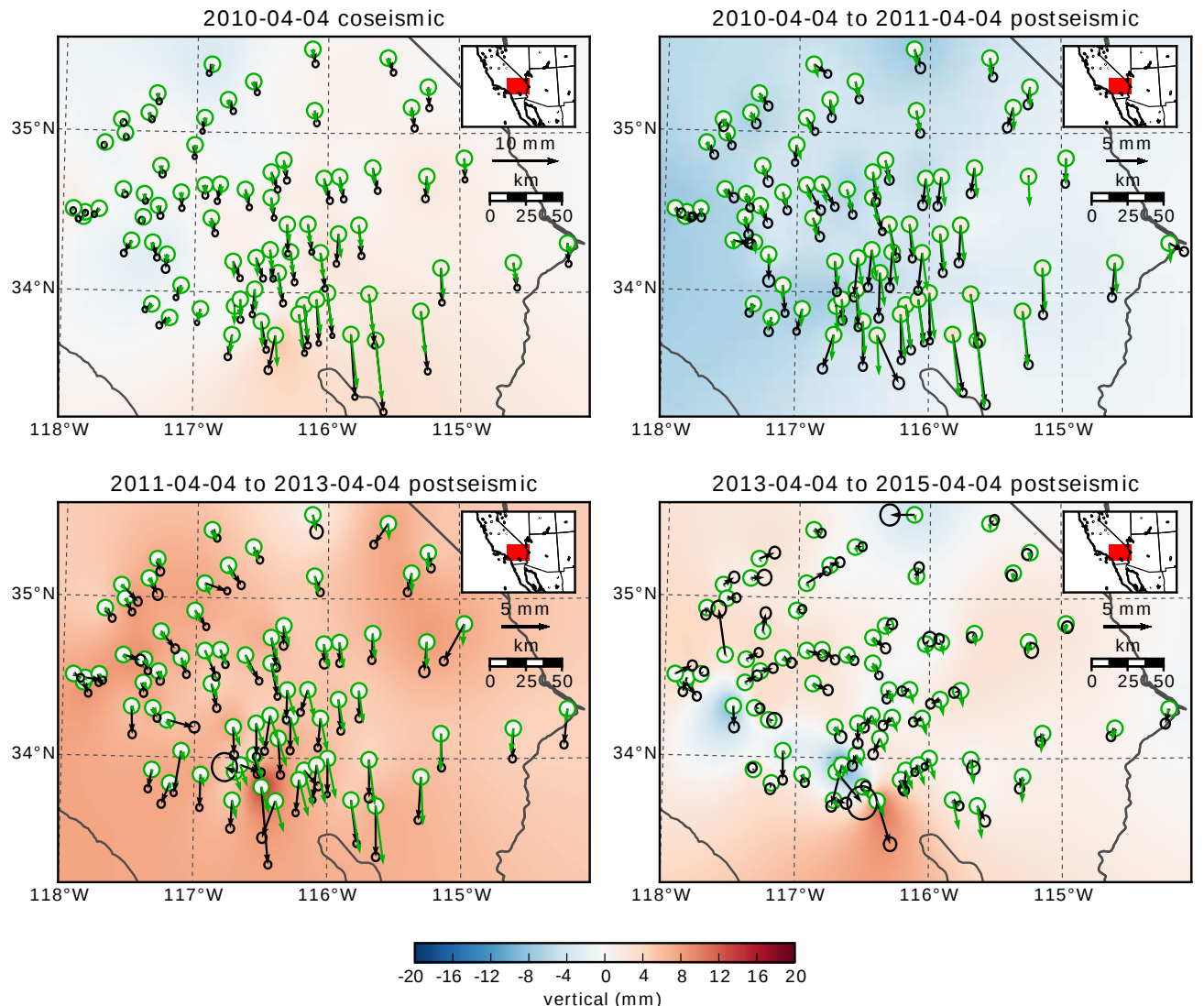
240 We estimate coseismic and time-dependent postseismic fault slip, both of which are as-
 241 sumed to occur on a fault geometry modified from Wei *et al.* [2011b]. Field studies [Fletcher
 242 *et al.*, 2014] and LIDAR observations [Oskin *et al.*, 2012] have revealed a significantly more
 243 complicated fault geometry than what was inferred by Wei *et al.* [2011b], especially within the
 244 Sierra Cucapah. However, we find that a relatively simple coseismic fault geometry based on



215 **Figure 4.** Near-field coseismic and cumulative postseismic displacements over the indicated time periods
 216 (black) and predicted displacements for our preferred model from Section 3.3 (green). The black error ellipses
 217 show the 68% confidence interval for the observed horizontal displacements. Observed vertical displacements
 218 are shown as an interpolated field and predicted vertical displacements are shown within the green circles.
 219 Note that the interpolant is not well constrained in Mexico where there is no data available.

depth (km)	λ (GPa)	μ (GPa)	η_{eff} (10^{18} Pa s)	μ_k/μ
0-5	24.0	24.0	-	-
5-15	35.0	35.0	-	-
15-30	42.0	42.0	44.3	0.0
30-60	61.0	61.0	5.91	0.375
60-90	61.0	61.0	1.99	0.375
90-120	61.0	61.0	1.31	0.375
120-150	61.0	61.0	1.10	0.375
150-∞	61.0	61.0	1.07	0.375

230 **Table 1.** Assumed and estimated material properties. λ and μ are assumed known *a priori* and are based
 231 on the values used for the coseismic model by Wei *et al.* [2011b]. The values for η_{eff} are estimated in Section
 232 3.2, and μ_k/μ are the optimal shear moduli ratios found in Section 3.3 for a Zener rheology upper mantle.

**Figure 5.** Same as Figure 4 but for far-field stations.

[Wei *et al.*, 2011b] is adequate because most of the stations used in this study are sufficiently far from the El Mayor-Cucapah rupture that they are insensitive to the details in the fault geometry found by Fletcher *et al.* [2014] and Osokin *et al.* [2012]. The fault geometry used in this study (Figure 1) consists of the two main fault segments inferred by Wei *et al.* [2011b], where the northern segment runs through the Sierra Cucapah up to the US-Mexico border and the southern segment is the Indiviso fault which extends down to the Gulf of California. Both segments extend from the surface to 15 km depth. We extend the northern segment by 40 km to the northwest, which is motivated by the clustering of aftershocks on the northern tip of the coseismic rupture zone [Hauksson *et al.*, 2011; Kroll *et al.*, 2013]. This extended fault segment was also found to be necessary by Rollins *et al.* [2015] and Pollitz *et al.* [2012] in order to describe the postseismic deformation.

256 3.1 Elastic Postseismic Inversion

We consider a variety of rheologic models for the lower crust and upper mantle. The simplest rheologic model is to consider them to be effectively elastic and isotropic. In such case, the rheologic parameters consist of the reasonably well known Lamé parameters, λ and μ , and we use the same values used by Wei *et al.* [2011b] throughout this paper (Table 1). The only unknown is the distribution of fault slip, which can be estimated from postseismic deformation through linear least squares. Rollins *et al.* [2015] used a subset of the GPS stations considered in this study and found that three years of postseismic deformation following the El Mayor-Cucapah earthquake can be explained with afterslip on the coseismic fault plane without requiring any viscoelastic relaxation. We also perform an elastic slip inversion, but we use GPS stations within a larger radius about the El Mayor-Cucapah epicenter (400 km instead of \sim 200 km). Our forward problem describing predicted postseismic deformation, u_{pred} , in terms of time dependent fault slip, s , is

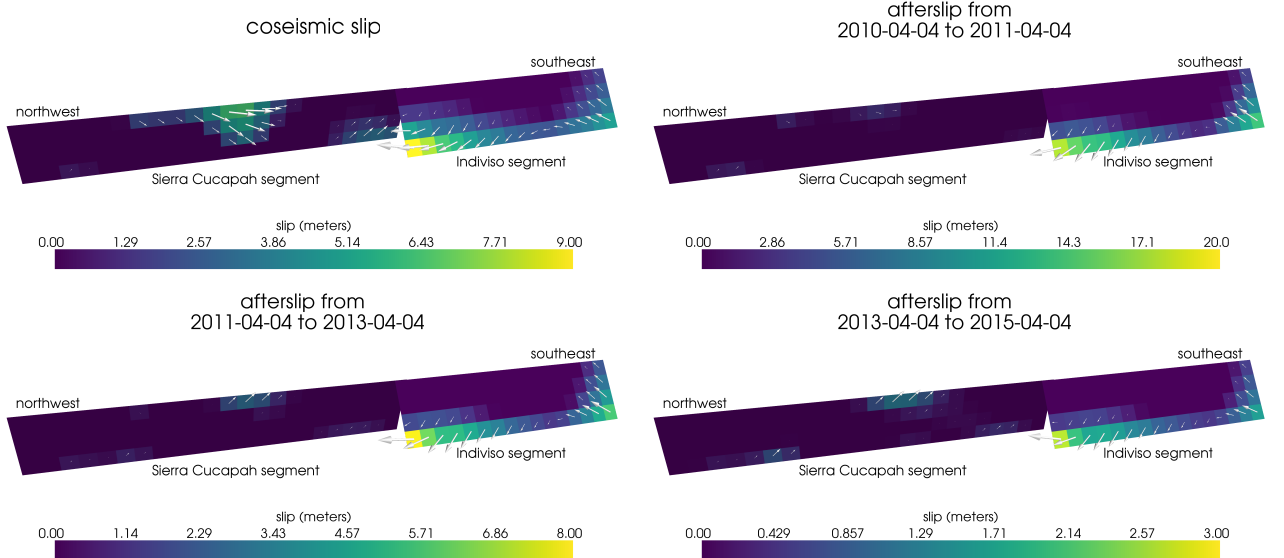
$$268 \quad u_{\text{pred}}(x, t) = \int_F s(\xi, t) g(x, \xi) d\xi, \quad (9)$$

where F denotes the fault and $g(x, \xi)$ is the elastic Green's function describing displacement at surface position x resulting from slip at ξ on the fault. We estimate coseismic slip and the rate of afterslip over the postseismic time intervals 0.0-0.125, 0.125-0.25, 0.25-0.5, 0.5-1.0, 1.0-2.0, 2.0-3.0, 3.0-4.0, and 4.0-5.0 years. Each fault segment is discretized into roughly 4 km by 4 km patches and we impose that the direction of slip and slip rate are within 45° of right-lateral. We also add zeroth-order Tikhonov regularization so that our solution for s satisfies

$$275 \quad \min_s \left(\left\| \frac{u_{\text{pred}}(s) - u_{\text{post}}}{\sigma_{\text{post}}} \right\|_2^2 + \lambda_s \|s\|_2^2 \right), \quad (10)$$

where σ_{post} is the uncertainty on postseismic displacements and λ_s is a penalty parameter which is chosen with a trade-off curve. We use Pylith [Aagaard *et al.*, 2013] to compute the Green's functions for this inversion as well as for the remaining inversions in this paper.

Our coseismic slip and afterslip solutions are shown in Figure 6. Similar to Rollins *et al.* [2015], we find that a large amount of afterslip on the Indiviso fault segment is required to explain the observations. The potency of our inferred coseismic slip is $3.2 \times 10^9 \text{ m}^3$, equivalent to a Mw=7.28 earthquake when assuming a shear modulus of 32 GPa. The potency of our inferred cumulative five years of afterslip is $6.1 \times 10^9 \text{ m}^3$, equivalent to a Mw=7.46 earthquake, which is unrealistically large if we consider afterslip to be driven by coseismically induced stresses. Figure 7 shows the time series for the observed and predicted postseismic displacements at stations along the El Mayor-Cucapah P-axis. We show the radial component of displacements with respect to the El Mayor-Cucapah epicenter and we also rescale the displacements so that the difference between the minimum and maximum observed displacements are the same for each station. Our elastic slip model accurately describes near-field postseis-



295 **Figure 6.** Coseismic slip and cumulative afterslip over the indicated time intervals when assuming the crust
296 and mantle are elastic. Color indicates the magnitude of slip and arrows indicate the motion of the hanging
297 wall.

290 mic deformation and systematically underestimates postseismic deformation at epicentral dis-
291 tances $\gtrsim 150$ km. When the fault segments used in the inversion are extended down to 30 km
292 depth, rather than 15 km, the systematic far-field residuals are smaller but remain apparent.
293 Because an elastic model requires an unrealistic amount of afterslip and is unable to predict
294 far-field deformation, we move on to consider viscoelastic models in the next section.

307 3.2 Early Postseismic Inversion

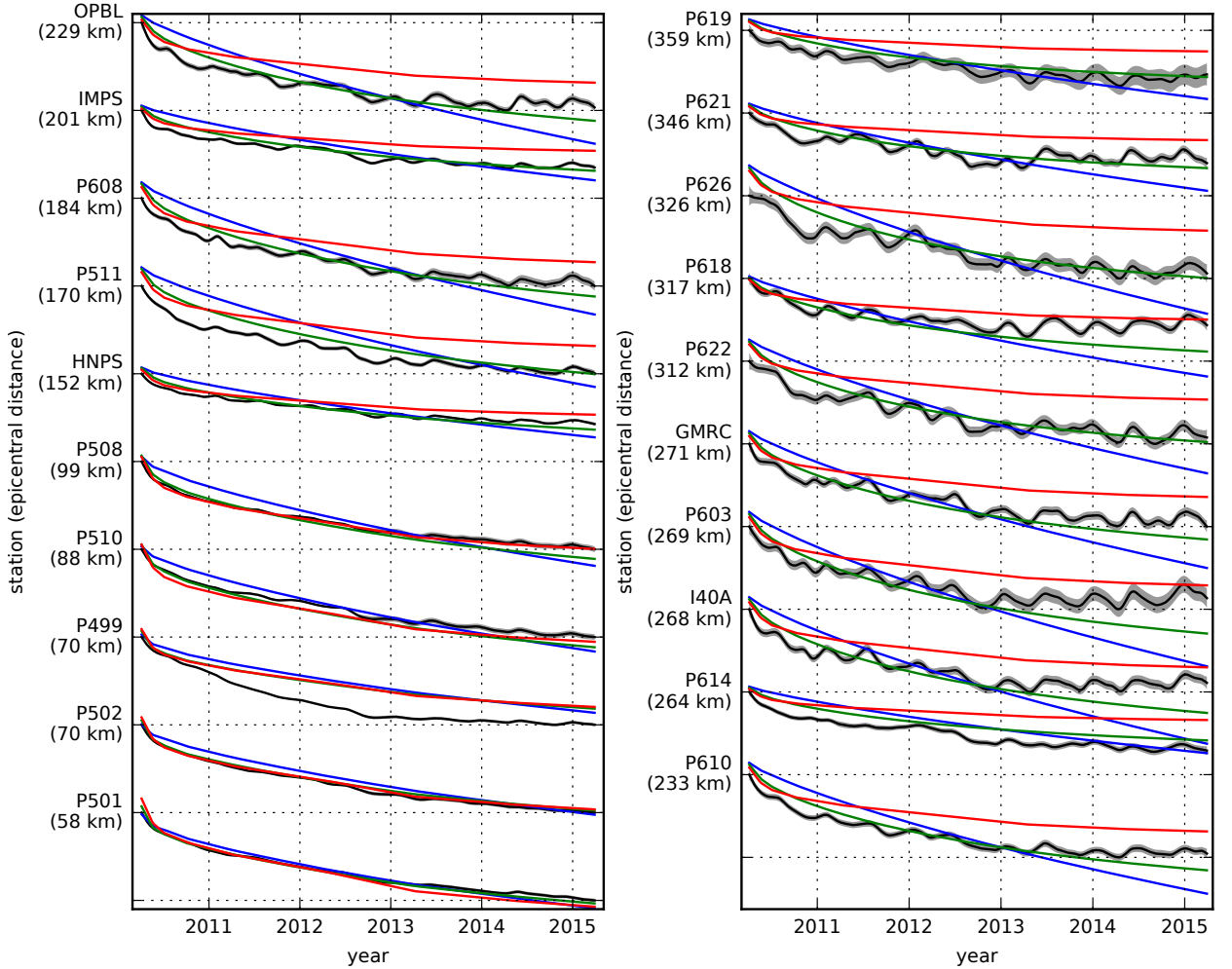
308 For any linear viscoelastic rheology of the crust and mantle, postseismic displacements
309 resulting from time dependent fault slip can be described as

$$310 u_{\text{pred}}(x, t) = \int_F s(\xi, t) g(x, \xi) d\xi + \int_0^t \int_F s(\xi, \tau) f(t - \tau, x, \xi) d\xi d\tau, \quad (11)$$

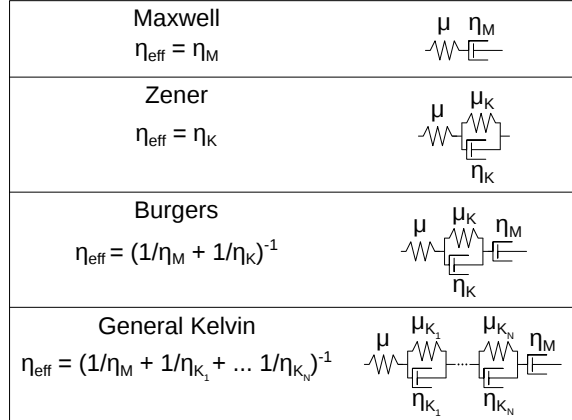
311 where $f(t, x, \xi)$ describes the time-dependent velocity at x resulting from viscoelastic relax-
312 ation of stresses induced by slip at ξ . f is a function of λ , μ , and any additional rheologic pa-
313 rameters controlling the viscoelastic response, which are generally not well known. Schematic
314 representations of the viscoelastic rheologic models considered in this study are shown in Figure 8. We discuss these rheologic models and their use in geophysical studies in Section 4.

317 In order to greatly simplify the inverse problem, we use the method described in *Hines*
318 and *Hetland* [2016] to constrain an initial effective viscosity structure from the early postseis-
319 mic deformation. Our method uses the fact that coseismic stresses throughout the crust and
320 upper mantle depend on the instantaneous elastic parameters and are independent of the vis-
321 coelastic parameters which we wish to estimate. Immediately following an earthquake, each
322 parcel will have a strain rate that is proportional to the coseismic stress and inversely propor-
323 tional to the parcel's effective viscosity, η_{eff} . Using one-dimensional rheologic models, we de-
324 fine the effective viscosity as

$$325 \eta_{\text{eff}} = \frac{\sigma}{\dot{\varepsilon}} \Big|_{t=0}, \quad (12)$$



298 **Figure 7.** Scaled radial component of postseismic displacements. Downward motion indicates that the
 299 station is moving toward the El Mayor-Cucapah epicenter. Displacement time series are scaled so that the
 300 minimum and maximum observed values lie on the grid lines. The observed postseismic displacements, u_{post}
 301 are shown in black with gray indicating the 68% confidence interval. The displacements predicted by the best
 302 fitting elastic model are shown in red. The blue and green lines are the predicted postseismic displacements
 303 for the models discussed in Section 3.3. The blue lines show the predicted displacements for the model with
 304 a Maxwell viscoelastic lower crust and upper mantle. The green line shows the predicted displacements
 305 for the model with a Maxwell viscoelastic lower crust and a Zener viscoelastic upper mantle. The effective
 306 viscosities are the same for both models and are shown in Figure 12.



315 **Figure 8.** Schematic illustration of the rheologic models considered in this paper as well as their effective
 316 viscosities.

325 where σ is an applied stress at $t = 0$ and $\dot{\varepsilon}$ is the resulting strain rate. Figure 8 shows how
 326 η_{eff} relates to the parameters for various linear viscoelastic rheologies. We can deduce that the
 327 initial rate of surface deformation resulting from viscoelastic relaxation is a summation of the
 328 surface deformation resulting from relaxation in each parcel, scaled by the reciprocal of the
 329 parcel's effective viscosity. That is to say

$$f(0, x, \xi) = \int_L \frac{h(x, \xi, \zeta)}{\eta_{\text{eff}}(\zeta)} d\zeta, \quad (13)$$

330 where L denotes the crust and mantle and $h(x, \xi, \zeta)$ describes the initial rate of deformation
 331 resulting from viscoelastic relaxation at ζ induced by slip at ξ . We can combine eq. (13) with
 332 eq. (11) to get a first-order approximation for early postseismic deformation,

$$u_{\text{pred}}(x, t) \approx \int_F s(\xi, t) g(x, \xi) d\xi + \int_0^t \int_F \int_L \frac{s(\tau, \xi)}{\eta_{\text{eff}}(\zeta)} h(x, \xi, \zeta) d\zeta d\xi d\tau, \quad (14)$$

333 which is valid for as long as the rate of deformation resulting from viscoelastic relaxation is
 334 approximately constant. Although eq. (14) may only be valid for a short portion of the post-
 335 seismic period, its utility becomes apparent when noting that g and h are only functions of
 336 the fault geometry and instantaneous elastic properties, λ and μ , and thus g and h can be com-
 337 puted numerically as a preprocessing step. The forward problem in eq. (14) can then be rapidly
 338 evaluated for any realization of s and η_{eff} . This is in contrast to evaluating the full forward
 339 problem, eq. (11), numerically for each realization of s and the unknown rheologic proper-
 340 ties.

341 Details on how eq. (14) is used to estimate s and η_{eff} from postseismic deformation can
 342 be found in *Hines and Hetland* [2016]. A non-linear Kalman filter based inverse method can
 343 also be used to estimate s and η_{eff} in a manner similar to *Segall and Mathews* [1997] or *McGuire*
 344 and *Segall* [2003], in which we would not have to explicitly impose a time dependent parametriza-
 345 tion of s . We have thoroughly explored Kalman filter based approaches, but we ultimately pre-
 346 fer the method described in *Hines and Hetland* [2016] because of its relative simplicity. More-
 347 over, we believe the piecewise continuous representation of slip with respect to time is suf-
 348 ficiently general for the resolving power of these GPS data.

349 We estimate coseismic slip and afterslip with the same spatial and temporal discretiza-
 350 tion as in Section 3.1. Simultaneously, we estimate η_{eff} within six vertically stratified layers
 351 which have depths ranging from 15-30 km, 30-60 km, 60-90 km, 90-120 km, 120-150 km,

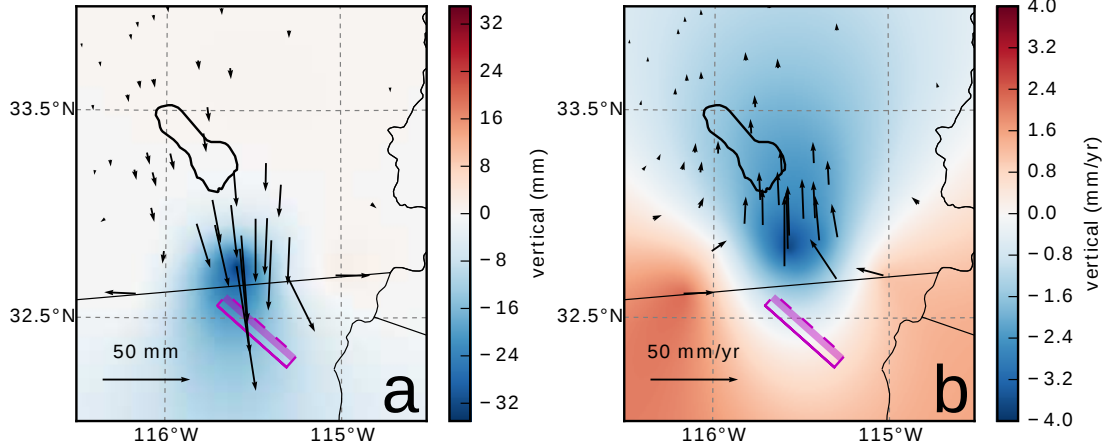
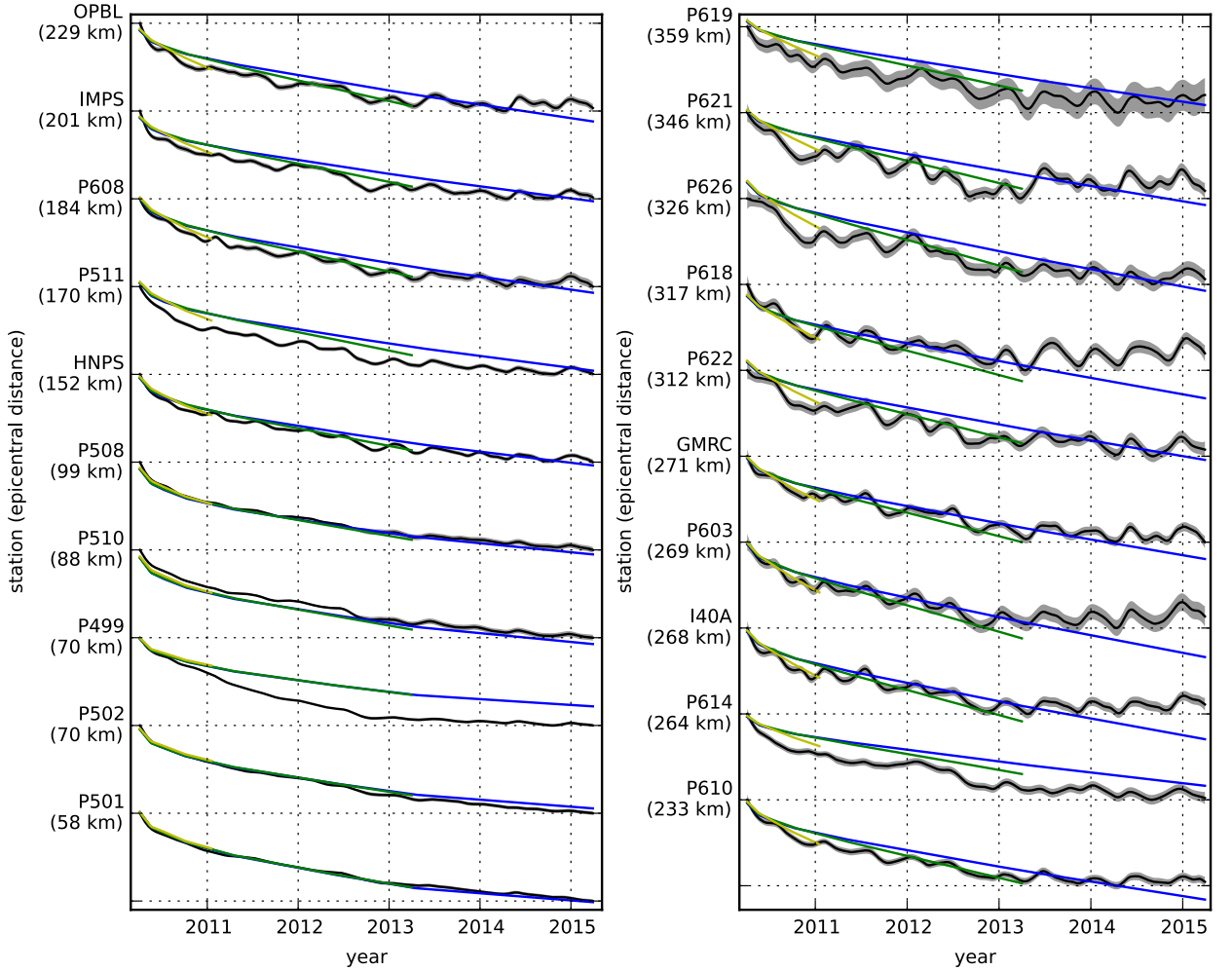


Figure 9. Displacements resulting from fault slip at lower crustal depths (a), and initial velocities resulting from subsequent relaxation of a viscoelastic lower crust (b). The fault segment dips 75° to the north-east and its surface projection is outlined in magenta. The highlighted area on the fault extends from 15 to 30 km depth and indicates where 1 meter of right-lateral slip was imposed. The elastic properties of the crust and mantle are the same as in Table 1, and η_{eff} is 10^{18} Pa s in the lower crust. Vertical displacements are interpolated between station locations.

and from 150 km to the bottom of our numerical model domain at 800 km. We again restrict fault slip to occur between 0 and 15 km depth, which is done in order to help eliminate inevitable non-uniqueness in the inversion. It is well understood that fault slip at sufficiently great depths can produce surface deformation that is indistinguishable from viscoelastic relaxation, at least in two-dimensional earthquake models [Savage, 1990]. Additionally, we note that when simultaneously estimating both afterslip and viscosity in the lower crust, the inverse problem becomes particularly ill-posed. This ill-posedness is illustrated in Figure 9, which shows the displacements resulting from a meter of slip on a fault extending from 15 to 30 km depth and the initial velocity resulting from subsequent viscoelastic relaxation in the lower crust, which is given a viscosity of 10^{18} Pa s. In this demonstration, the viscoelastic relaxation is entirely driven by the fault slip in the lower crust. The horizontal displacements from fault slip are in the opposite direction as the displacements resulting from viscoelastic relaxation. This means that surface displacements resulting from afterslip at lower crustal depths can be cancelled out, at least partially, by a low viscosity lower crust. We eliminate this null space by allowing only one mechanism in the lower crust, which we choose to be viscoelastic relaxation. This is not to say that we do not believe deep afterslip is a possibility; rather, we restrict slip to seismogenic depths as a modeling necessity. Although, it has been noted that the pattern of vertical postseismic deformation following the El Mayor-Cucapah earthquake indicates that a significant amount of afterslip must be shallow [Rollins *et al.*, 2015].

We must determine at which point the early postseismic approximation breaks down, which we will denote as t_{bd} . As noted, eq. (14) is valid for as long as the rate of deformation resulting from viscoelastic relaxation is approximately constant. We can almost certainly assume that deformation at the most far-field stations, which are ~ 400 km away from the El Mayor-Cucapah epicenter, is the result of viscoelastic relaxation. The approximation should then be valid for as long as a linear trend adequately approximates the far-field deformation. Using this logic, it would appear that t_{bd} is about one year after the El Mayor-Cucapah earthquake. Another way to determine t_{bd} is to find the best fitting prediction of eq. (14) to observed deformation using increasing durations of the postseismic time series. t_{bd} should be the point when eq. (14) is no longer capable of describing the observed deformation without incurring systematic misfits. When using eq. (14) to fit the entire five years of postseismic displacements,



399 **Figure 10.** Observed postseismic displacements (black) and best fitting predictions of eq. (14) to 5.0 (blue),
400 3.0 (green), and 0.8 (yellow) years of the postseismic data.

388 we see that the near-field displacements (e.g., station P501) are accurately predicted. When
389 looking at displacements in the far-field (e.g., station P621), we see that eq. (14) overestimates
390 the rate of deformation in the later postseismic period and underestimates the rate of defor-
391 mation in the early period (Figure 10). Due to the low signal-to-noise ratios for far-field sta-
392 tions, it is difficult to determine at what point eq. (14) is no longer able to predict the observed
393 displacements; however, we settle on $t_{bd} = 0.8$ years after the earthquake, while acknowl-
394 edging that the choice is subjective. As noted in *Hines and Hetland* [2016], overestimating t_{bd}
395 will result in a bias towards overestimating η_{eff} , while picking a t_{bd} which is too low will not
396 necessarily result in a biased estimate of η_{eff} , although the uncertainties would be larger. We
397 can then consider inferences of η_{eff} to be an upper bound on the viscosity needed to describe
398 the far-field rate of deformation during the first 0.8 years of postseismic deformation.

401 We estimate coseismic slip, afterslip, and effective viscosities by solving

$$\min_{s, \eta_{eff}} \left(\left\| \frac{u_{pred}(s, \eta_{eff}) - u_{post}}{\sigma_{post}} \right\|_2^2 + \lambda_s \|s\|_2^2 + \lambda_\eta \|\nabla \eta_{eff}^{-1}\|_2^2 \right), \quad (15)$$

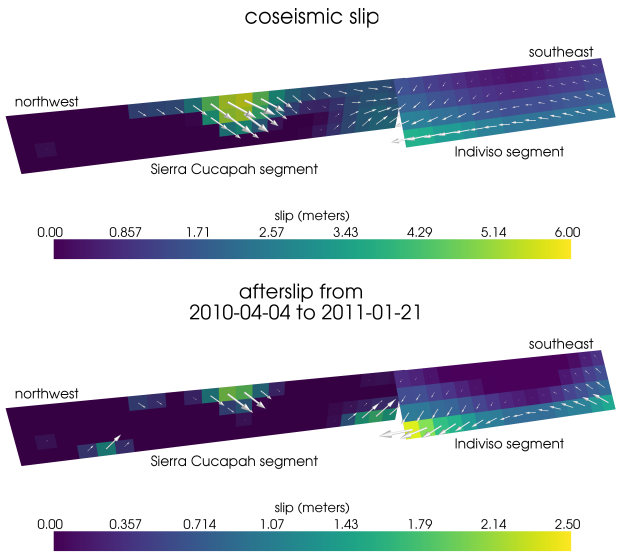
402 where u_{post} consists of the first 0.8 years of postseismic deformation and u_{pred} are the pre-
 403 dicted displacements from eq. (14). Due to inherent non-uniqueness, we have added zeroth-
 404 order Tikhonov regularization to estimates of s and second-order Tikhonov regularization to
 405 estimates of effective fluidity η_{eff}^{-1} . The degree to which we impose the regularization on slip
 406 and fluidity is controlled by the penalty parameters λ_s and λ_η , which are chosen with trade-
 407 off curves (Figure S1). Our goal is to get a prior constraint on η_{eff} to minimize the amount
 408 of searching we have to do when describing the postseismic deformation over the full five years,
 409 which we do in Section 3.3. Estimates of s made here will not be used in Section 3.3, and
 410 so the motivation behind adding regularization to s is to ensure that the slip driving viscoelas-
 411 tic relaxation in eq. (14) is sensible.

412 Our initial estimate for coseismic slip and cumulative afterslip over the first 0.8 years
 413 after the El Mayor-Cucapah earthquake are shown in Figure 11. Similar to our elastic slip model
 414 from Section 3.1, a significant amount of right-lateral and normal coseismic slip is inferred
 415 to be on the Sierra Cucapah segment. Our coseismic slip solution on the Sierra Cucapah seg-
 416 ment is consistent with field studies [Fletcher *et al.*, 2014] and the model from Wei *et al.* [2011b].
 417 Our inferred slip on the Indiviso fault segment differs from Wei *et al.* [2011b] because the GPS
 418 data used in this study is not capable of resolving the spatial distribution of fault slip on that
 419 segment (Figure S2). The potency of inferred coseismic slip is $3.3 \times 10^9 \text{ m}^3$, which is also
 420 about the same as that inferred from Section 3.1. The present inference of afterslip on the In-
 421 diviso fault is significantly less than what was found in the Section 3.1 where we did not ac-
 422 count for viscoelasticity. When fault slip is simultaneously estimated with viscosity, the po-
 423 tency of inferred afterslip over the first 0.8 years after the earthquake is $0.85 \times 10^9 \text{ m}^3$, com-
 424 pared to $3.5 \times 10^9 \text{ m}^3$ when we assume the crust and upper mantle are elastic. The signifi-
 425 cant amount of afterslip inferred on the Indiviso fault in Section 3.1 seems to be compensat-
 426 ing for unmodeled viscoelastic relaxation. The fact that there is still an appreciable amount
 427 of afterslip inferred on the Indiviso fault raises the question of whether it is compensating for
 428 viscoelastic relaxation that is more localized than what we allow for since we only estimate
 429 depth dependent variations in viscosity.

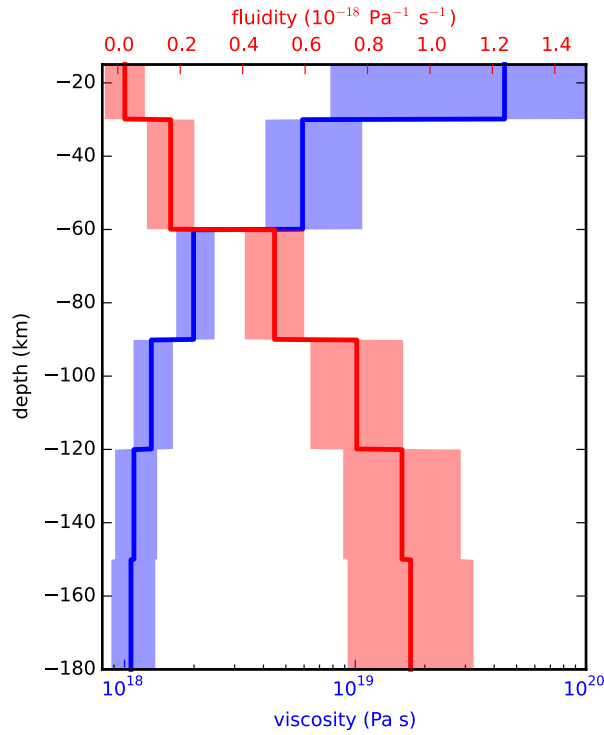
430 Our estimated effective viscosities, and corresponding fluidities, are shown in Figure 12.
 431 Although fluidity is rarely used in geophysical literature, eq. (13) is linear with respect to flu-
 432 idity and so the fluidity indicates the amplitude of the viscoelastic signal coming from each
 433 layer. We use bootstrapping to find the 95% confidence intervals for our estimated effective
 434 viscosities which are shown as shaded regions in Figure 12. It is important to remember that
 435 the presented effective viscosities were estimated with a smoothing regularization constraint
 436 and so the uncertainties are almost certainly underestimated [Aster *et al.*, 2011]. Indeed, many
 437 viscosity profiles which are outside of the shown confidence intervals can just as adequately
 438 described the first 0.8 years of postseismic deformation. Our solution in Figure 12 should be
 439 interpreted as the smoothest effective viscosity profile which is capable of describing the data.
 440 This means that any sharp viscosity transitions will be tapered out in the inversion, which we
 441 demonstrate with a synthetic test in Figure S2. Nonetheless, a robust feature that we see with
 442 a variety of choices for λ_s , λ_η , and t_{bd} is that the largest jump in fluidity is at 60 km depth,
 443 which is consistent with the range of lithosphere-asthenosphere boundary depths inferred by
 444 Lekic *et al.* [2011]. This transitional depth is also consistent with the the viscosity structure
 445 required to explain far-field postseismic deformation following the Hector Mine earthquake
 446 [Freed *et al.*, 2007]. We find that the viscosity below 60 km depth needs to be $\sim 1 \times 10^{18} \text{ Pa}$
 447 s to describe the early rate of postseismic deformation at far-field stations while the lower crust
 448 and uppermost mantle need to be relatively stronger. The viscosity of the lower crust has the
 449 largest uncertainties because there is no evidence of relaxation in that layer, meaning that it
 450 is effectively elastic over the first 0.8 years after the earthquake.

456 3.3 Full Postseismic Inversion

457 In the previous section, we used the inverse method from Hines and Hetland [2016] to
 458 constrain the effective viscosity structure required to explain the first 0.8 years of postseismic



451 **Figure 11.** Coseismic slip and afterslip inferred by fitting eq. (14) to the first 0.8 years of postseismic
452 displacements.



453 **Figure 12.** Effective viscosities and associated fluidities inferred by fitting eq. (14) to the first 0.8 years of
454 postseismic displacements. 95% confidence intervals, estimated from bootstrapping, are indicated by shaded
455 regions.

459 deformation. In this section, we use these effective viscosities as a prior constraint when searching
 460 for models which are capable of describing the available five years of postseismic data,
 461 where our forward problem is now eq. (11) rather than the approximation given by eq. (14).
 462 We perform a series of fault slip inversions assuming a variety of rheologies for the lower crust
 463 and upper mantle which are consistent with our findings from Section 3.2. We appraise each
 464 model using the mean chi-squared value,

$$\bar{\chi}^2 = \frac{1}{N} \left\| \frac{u_{\text{pred}} - u_{\text{post}}}{\sigma_{\text{post}}} \right\|_2^2, \quad (16)$$

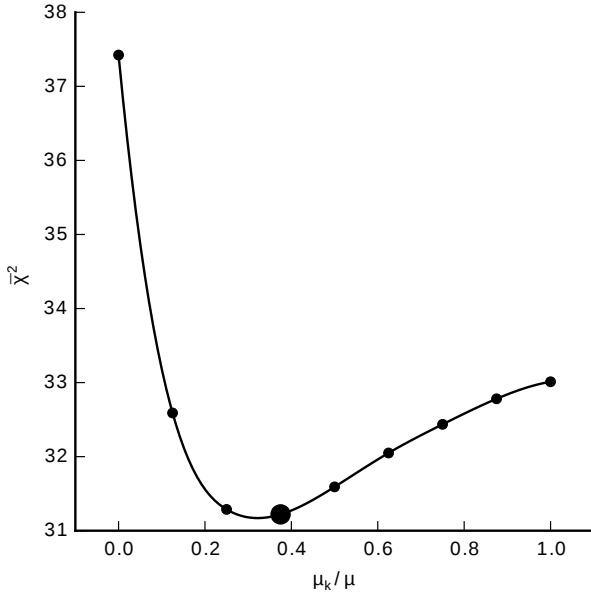
465 where N is the number of observations.

466 We first assume that the crust and mantle can be described with a Maxwell rheology,
 467 and we set the steady-state viscosity, η_M , equal to our inference of η_{eff} . We compute f and
 468 g from eq. (11) using Pylith, and we use the same spatial and temporal discretization of s as
 469 in Sections 3.1 and 3.2. We estimate s using linear least squares and find a misfit of $\bar{\chi}^2 =$
 470 37.4. For comparison, $\bar{\chi}^2 = 35.3$ for the elastic model from Section 3.1. The Maxwell vis-
 471 coelastic model has a larger misfit because it tends to overestimate the rate of deformation af-
 472 ter about three years (Figure 7). Since our initial estimates of η_{eff} may be biased towards over-
 473 estimating viscosities, we have also performed the slip inversion where we use uniformly lower
 474 viscosities in the crust and mantle; however, decreasing the viscosity only increases the mis-
 475 fit. Although, the viscosities used here are consistent with the successful Maxwell viscoelas-
 476 tic models found by *Rollins et al.* [2015] and *Spinler et al.* [2015], which had mantle viscosi-
 477 ties on the order of 10^{18} Pa s and relatively higher lower crustal viscosities, we find that such
 478 a model is incapable of describing the entire postseismic time series. *Pollitz et al.* [2001] sim-
 479 ilarly recognized this deficiency in a Maxwell rheology, which then motivated their exploration
 480 of a Burgers rheology upper mantle [*Pollitz*, 2003].

481 Instead of exploring a Burgers rheology mantle, which introduces two new parameters
 482 that need to be estimated, the transient viscosity, η_K , and transient shear modulus, μ_K , we first
 483 consider a Zener rheology for the mantle, which only introduces one unknown model param-
 484 eter, μ_K . We assume that the lower crust still has a Maxwell rheology. The steady-state vis-
 485 cosity in the crust and the transient viscosity in the mantle are set equal to the inferred effec-
 486 tive viscosities. We then estimate the ratio of shear moduli, $\frac{\mu_K}{\mu}$. We compute nine different
 487 sets of Green's functions, f and g , where we assume values of $\frac{\mu_K}{\mu}$ ranging from 0 to 1. The
 488 former being a degenerate case where the Zener model reduces to the above Maxwell model.
 489 We estimate coseismic slip and afterslip for each realization of $\frac{\mu_K}{\mu}$. We find that a shear mod-
 490 uli ratio of 0.375 yields the best prediction to the observed postseismic displacements with a
 491 misfit of $\bar{\chi}^2 = 31.2$ (Figure 13). The improvement in the Zener model over the Maxwell model
 492 can be seen in the fit to the far-field data (Figure 7) where the Zener model does a significantly
 493 better job at explaining the transient rate of deformation throughout the five years considered
 494 in this study. The rheologic parameters for our preferred Zener model are summarized in Ta-
 495 ble 1.

496 Because we are able to adequately describe the available five years of postseismic de-
 497 formation with a Zener model, we do not find it necessary to explore the parameter space for
 498 a more complicated Burgers rheology. However, since the Zener model is a Burgers model with
 499 an infinite steady-state viscosity, we can conclude that any Burgers rheology that has a tran-
 500 sient viscosity consistent with that found in Section 3.2 and a steady-state viscosity $\gtrsim 10^{20}$
 501 Pa s, which is effectively infinite on the time scale of five years, would also be able to sat-
 502 isfactorily describe the observable postseismic deformation.

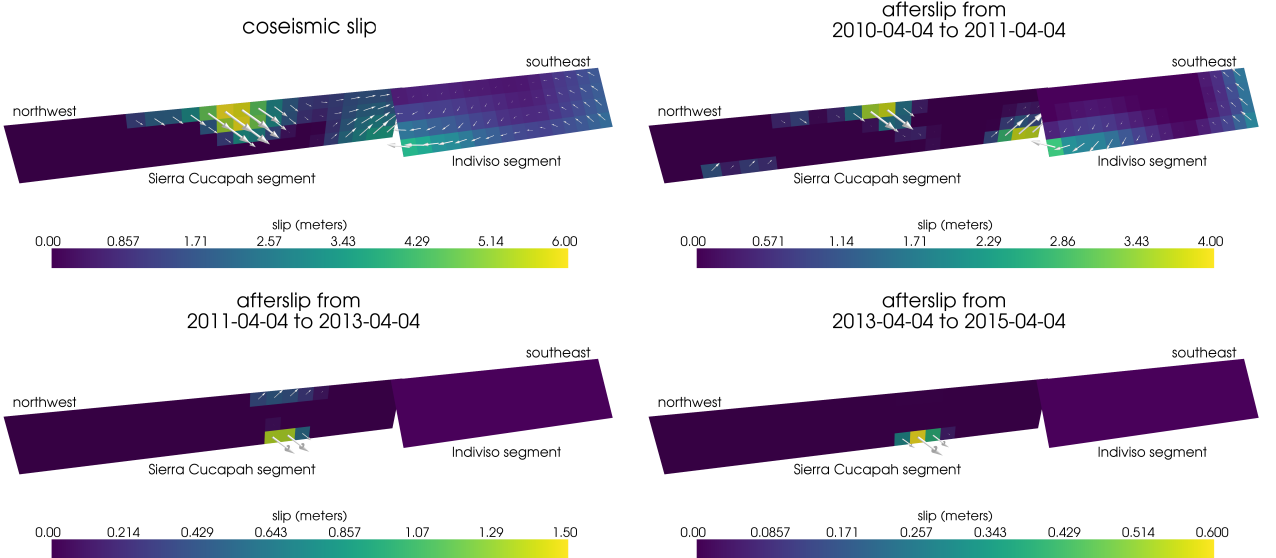
503 The regularized inference of coseismic slip and afterslip for our preferred Zener model
 504 is shown in Figure 14. The inferred coseismic potency is 3.0×10^9 m³, equivalent to a Mw=7.26
 505 earthquake, where most of the slip is shallow and on the Sierra Cucapah fault segment. The
 506 potency of five years of afterslip is 1.1×10^9 m³. Most of the afterslip in our preferred model
 507 occurs within the first year after the earthquake and coincides with the location of our inferred



496 **Figure 13.** Mean chi-squared value for the best fitting slip model as a function of the transient shear modu-
 497 lus relative to the elastic shear modulus in a Zener upper mantle. Large dot indicates our preferred ratio.

510 coseismic slip. Inferred afterslip within the first year is accounting for the most rapid near-
 511 field transient deformation (Figure S3). After one year, afterslip is inferred to be deeper down
 512 on the Sierra Cucapah segment, which is describing some of the sustained near-field postseis-
 513 mic deformation. We emphasize, that the GPS station closest to where we infer afterslip, P496,
 514 is still about 30 km away, which is too far for us to conclusively argue for sustained localized
 515 deformation rather than shallow distributed deformation. The deep afterslip inferred after one
 516 year could potentially be describing deformation resulting from lower crustal flow. To test this,
 517 we have modified our preferred model by decreasing the lower crustal viscosity from $5.91 \times$
 518 10^{19} Pa s to 1×10^{19} Pa s, which is still consistent with our viscosity inference from Sec-
 519 tion 3.2, and we inverted for fault slip. We find that a model with a weaker lower crust ad-
 520 equately describes the postseismic displacements without any afterslip after one year, while
 521 still requiring about the same amount of afterslip over the first year. We do believe that the
 522 early, shallow afterslip on the Sierra Cucapah segment is a robust feature in our preferred model,
 523 while we are not confident in our inference of later deep afterslip.

524 The postseismic displacements predicted by our preferred Zener model are shown in Fig-
 525 ures 4, 5 and 7. The largest misfit occur within the Imperial Valley and there does not appear
 526 to be any systematic trend in the residuals. This suggests that the large errors are due to lo-
 527 calized processes such as fault slip in the Imperial Valley triggered by the El Mayor-Cucapah
 528 earthquake [Wei *et al.*, 2011a, 2015]. We do not see any pattern in the residuals that would sug-
 529 gest a laterally heterogeneous viscosity structure, which has been explored by Pollitz *et al.* [2012]
 530 and Rollins *et al.* [2015]. We do notice regionally uniform seasonal oscillations in the lateral
 531 and vertical components of the residuals with an amplitude of 1-2 millimeters. This is the re-
 532 result of our method for data processing which is not able to completely remove the seasonal
 533 signal in the GPS data, which was discussed in Section 2. Additionally, we see systematic mis-
 534 fit in the later postseismic period west of the Landers and Hector Mine earthquakes, which may
 535 be the result of unmodeled postseismic deformation following those earthquakes. Lastly, there
 536 are clear discrepancies between the observed and predicted vertical displacements following
 537 the first year after the El Mayor-Cucapah earthquake. We observe a broad uplift throughout
 538 Southern California which is inconsistent with any postseismic model.



539 **Figure 14.** Inferred coseismic slip and afterslip when assuming a Maxwell rheology in the lower crust and
 540 a Zener rheology in the upper mantle. The transient viscosity, η_K , in the mantle and steady-state viscosity,
 541 η_M , in the crust are set equal to the effective viscosities from Figure 12. We use $\frac{\mu_K}{\mu} = 0.375$ in the upper
 542 mantle.

543 4 Discussion

544 It has long been recognized that deep afterslip and viscoelastic relaxation following an
 545 upper crustal earthquake can result in similar horizontal ground deformation at the surface [e.g.
 546 *Savage*, 1990; *Pollitz et al.*, 2001; *Hearn*, 2003; *Feigl and Thatcher*, 2006]. The similarity of
 547 the horizontal postseismic deformation results in a non-uniqueness in inferences of afterslip
 548 or viscoelastic relaxation. The spatial pattern of vertical postseismic deformation has been pro-
 549 posed to be a discriminant between deep afterslip and viscoelastic relaxation [e.g. *Pollitz et al.*,
 550 2001; *Hearn*, 2003]. It is, however, important to note that patterns of vertical deformation are
 551 very sensitive to the depth-dependence of viscosity below the upper crust [*Yang and Toksöz*,
 552 1981; *Hetland and Zhang*, 2014]. The similarity between deformation resulting from deep af-
 553 terslip and viscoelastic relaxation of coseismic stresses is different from the ill-posedness de-
 554 scribed in Section 3.2. In our method, any inferred afterslip will also mechanically drive ad-
 555 dditional viscoelastic relaxation. The horizontal deformation resulting from deep afterslip will
 556 generally be in the opposite direction as horizontal deformation resulting from viscoelastic re-
 557 laxation of subsequent stresses in the lower crust (Figure 9). As a result, there is a trade-off
 558 between inferences of deep afterslip and lower crustal viscosity. In our synthetic tests in *Hines*
 559 and *Hetland* [2016], we have found that inverting surface deformation for afterslip and vis-
 560 cosity within the same depth interval tends to result in overestimated afterslip and an under-
 561 estimated viscosity.

562 Most postseismic studies assume Maxwell viscoelasticity in the lower crust and upper
 563 mantle [e.g. *Nur and Mavko*, 1974; *Pollitz et al.*, 2000; *Hetland*, 2003; *Freed et al.*, 2006; *John-*
 564 *son et al.*, 2009; *Hearn et al.*, 2009], which is the simplest viscoelastic rheologic model. In South-
 565 ern California, postseismic studies following the Landers [*Pollitz et al.*, 2000], Hector Mine
 566 [*Pollitz et al.*, 2001], and El Mayor-Cucapah earthquake [*Spinler et al.*, 2015; *Rollins et al.*, 2015],
 567 have assumed Maxwell viscoelasticity in the lower crust and upper mantle and have inferred
 568 upper mantle viscosities on the order of 10^{17} to 10^{18} Pa s and lower crust viscosities $\gtrsim 10^{19}$
 569 Pa s. These postseismic studies are consistent with *Kaufmann and Amelung* [2000] and *Cav-*

570 alié *et al.* [2007], who found that an upper mantle viscosity of 10^{18} Pa s and a crustal viscosity
 571 $\gtrsim 10^{20}$ Pa s are necessary to describe subsidence resulting from changes in loading from
 572 Lake Mead. This isostatic adjustment is a process with similar spatial and temporal scales as
 573 postseismic deformation, and thus the inferred viscosities of these two types of studies would
 574 likely agree. While these studies found viscosities that are consistent with our effective vis-
 575 cosities from Section 3.2, they are inconsistent with viscosity estimates made from geophys-
 576 ical processes that occur over longer time scales. For example, Lundgren *et al.* [2009] found
 577 that lower crust and upper mantle viscosities on the order of 10^{21} and 10^{19} Pa s, respectively,
 578 are needed to describe interseismic deformation along the Southern San Andreas fault zone
 579 in the Salton Sea region. An even higher mantle viscosity, on the order of 10^{20} Pa s, is re-
 580 quired to describe isostatic adjustment resulting from the draining of Lake Bonneville, which
 581 occurs on the time scales of 10^4 years [Crittenden, 1967; Bills and May, 1987].

582 An additional deficiency with the Maxwell rheology is that it predicts a steady decay
 583 in the rate of postseismic deformation over time, which fails to describe the commonly ob-
 584 served rapid, early transience followed by a relatively steady rate of postseismic deformation.
 585 One could explain the early transient postseismic deformation with fault creep and the later
 586 phase with relaxation in a Maxwell viscoelastic lower crust and upper mantle [e.g Hearn *et al.*,
 587 2009; Johnson *et al.*, 2009]. However, postseismic deformation at distances greater than ~ 200
 588 km from the El Mayor-Cucapah epicenter can only be attributed to viscoelastic relaxation [e.g.
 589 Freed *et al.*, 2007] and we have demonstrated that the far-field deformation cannot be explained
 590 with a Maxwell rheology (Figure 7).

591 We found that a Zener rheology in the upper mantle with a transient viscosity of $\sim 10^{18}$
 592 Pa s does a noticeably better job at predicting far-field postseismic deformation. A general-
 593 ization of the Zener viscoelastic model, schematically represented as several Kelvin elements
 594 connected in series, is commonly used to describe seismic attenuation [Liu *et al.*, 1976]. The
 595 highest viscosity needed to describe seismic attenuation is on the order of 10^{16} Pa s [Yuen and
 596 Peltier, 1982] which has a characteristic relaxation time on the order of days. Even though
 597 our inferred transient viscosity is orders of magnitude larger than that required for seismic at-
 598 tenuation models, the two models are not incompatible. Rather, the delayed elasticity in seis-
 599 mic attenuation models occurs on such short time scales that it can be considered part of the
 600 instantaneous elastic phase of deformation associated with the preferred Zener model in this
 601 study.

602 Of course, a Zener rheology provides an incomplete description of the asthenosphere be-
 603 cause it does not have the fluid-like behavior required to explain isostatic rebound or convec-
 604 tion in the mantle [O'Connell, 1971]. Yuen and Peltier [1982] proposed a Burgers rheology
 605 with a low transient viscosity ($\eta_K \approx 10^{16}$ Pa s) and high steady-state viscosity ($\eta_M \approx 10^{21}$
 606 Pa s) to describe both seismic attenuation and long term geologic processes. The justification
 607 of a Burger's rheology mantle is further supported by laboratory experiments on olivine [Chopra,
 608 1997]. Pollitz [2003] sought to describe postseismic deformation following Hector Mine with
 609 a Burgers rheology mantle and they found a best fitting transient viscosity of 1.6×10^{17} Pa
 610 s and steady-state viscosity of 4.6×10^{18} Pa s. While the Burgers rheology was introduced
 611 as a means of bridging the gap between relaxation observed in long and short term geophys-
 612 ical processes, the inferred steady state viscosity from Pollitz [2003] is still inconsistent with
 613 the Maxwell viscosities inferred from studies on the earthquake cycle and Lake Bonneville.
 614 The transient viscosity inferred by Pollitz [2003] is constrained by the earliest phase of post-
 615 seismic deformation following the Hector Mine earthquake. While Pollitz [2003] ruled out deep
 616 afterslip as an alternative mechanism based on inconsistent vertical deformation, it is still pos-
 617 sible to successfully describe all components of early postseismic deformation following the
 618 Hector Mine earthquake with afterslip at seismogenic depths [Jacobs *et al.*, 2002]. It is then
 619 possible that the preferred rheologic model from Pollitz [2003] was biased towards inferring
 620 a particularly low transient viscosity by neglecting to account for afterslip. This is in contrast
 621 to the present study, where we have inferred a viscosity structure simultaneously with after-
 622 slip. We also argue that a transient rheology is necessary to explain postseismic deformation;

however, our preferred transient viscosity of $\sim 10^{18}$ Pa s in the upper mantle is an order of magnitude larger than the transient viscosity found by Pollitz [2003]. The transient viscosity inferred here is consistent with the results of Pollitz [2015], who reanalyzed postseismic data following the Landers and Hector Mine earthquake allowing the first few months of transient deformation to be described by afterslip. Since a Zener model is able to describe the available postseismic deformation following the El Mayor-Cucapah earthquake, any Burgers rheology with a steady-state viscosity that is $\gtrsim 10^{20}$ Pa s, effectively infinite over five years, would also be able to describe the postseismic deformation. Such a Burgers model might then be consistent with the steady-state viscosities necessary for lake loading, interseismic deformation, and mantle dynamics.

5 Conclusion

We have extracted a smoothed estimate of postseismic deformation following the El Mayor-Cucapah earthquake from GPS displacement time series. Our estimated postseismic deformation reveals far-field (epicentral distances $\gtrsim 200$ km) transient deformation which is undetectable after about three years. Near-field deformation exhibits transience that decays to a sustained, elevated rate after about one or two years. We found that near-field transient deformation can be explained with shallow afterslip, and the sustained rate of near-field deformation can either be explained with continued afterslip or viscoelastic relaxation in the lower crust. Far-field transient deformation can be more definitively ascribed to viscoelastic relaxation at depths greater than ~ 60 km. Beneath that depth, a transient viscosity of $\sim 1 \times 10^{18}$ Pa s is required to describe the rate of far-field deformation throughout the five years considered in this study. By describing the available postseismic deformation with a transient rheology in the mantle, our preferred model does not conflict with the generally higher steady-state viscosities inferred from geophysical processes occurring over longer time scales.

Acknowledgements

We thank Andy Freed for an illuminating discussion on the data used in this study. We also thank F. Pollitz and an anonymous reviewer for comments that improved this manuscript, and Editor Martha Savage. This material is based on EarthScope Plate Boundary Observatory data services provided by UNAVCO through the GAGE Facility with support from the National Science Foundation (NSF) and National Aeronautics and Space Administration (NASA) under NSF Cooperative Agreement No. EAR-1261833. The data used in this study can be found at www.unavco.org. This material is based upon work supported by the National Science Foundation under Grant Numbers EAR 1045372 and EAR 1245263.

References

- Aagaard, B. T., M. G. Knepley, and C. A. Williams (2013), A domain decomposition approach to implementing fault slip in finite-element models of quasi-static and dynamic crustal deformation, *Journal of Geophysical Research: Solid Earth*, 118, doi: 10.1002/jgrb.50217.
- Argus, D. F., M. B. Heflin, G. Peltzer, F. Crampé, and F. H. Webb (2005), Interseismic strain accumulation and anthropogenic motion in metropolitan Los Angeles, *Journal of Geophysical Research: Solid Earth*, 110(4), 1–26, doi:10.1029/2003JB002934.
- Aster, R. C., B. Borchers, and C. H. Thurber (2011), Parameter Estimation and Inverse Problems, vol. 90, Academic Press.
- Bawden, G. W., W. Thatcher, R. S. Stein, K. W. Hudnut, and G. Peltzer (2001), Tectonic contraction across Los Angeles after removal of groundwater pumping effects., *Nature*, 412(August), 812–815, doi:10.1038/35090558.
- Bills, B. G., and G. M. May (1987), Lake Bonneville: Constraints on Lithospheric Thickness and Upper Mantle Viscosity From Isostatic Warping of Bonneville, Provo, and

- 671 Gilbert Stage Shorelines, *Journal of Geophysical Research-Solid Earth and Planets*,
 672 92(B11), 11,493–11,508, doi:10.1029/JB092iB11p11493.
- 673 Çakir, Z., S. Ergintav, H. Özener, U. Dogan, A. M. Akoglu, M. Meghraoui, and
 674 R. Reilinger (2012), Onset of aseismic creep on major strike-slip faults, *Geology*,
 675 40(12), 1115–1118, doi:10.1130/G33522.1.
- 676 Cavalié, O., M. P. Doin, C. Lasserre, and P. Briole (2007), Ground motion measurement in
 677 the Lake Mead area, Nevada, by differential synthetic aperture radar interferometry time
 678 series analysis: Probing the lithosphere rheological structure, *Journal of Geophysical
 679 Research: Solid Earth*, 112(3), 1–18, doi:10.1029/2006JB004344.
- 680 Cetin, E., Z. Cakir, M. Meghraoui, S. Ergintav, and A. M. Akoglu (2014), Extent and
 681 distribution of aseismic slip on the Ismetpasa segment of the North Anatolian Fault
 682 (Turkey) from Persistent Scatterer InSAR, *Geochemistry, Geophysics, Geosystems*, 15,
 683 doi:10.1002/2014GC005307.Received.
- 684 Chopra, P. N. (1997), High-temperature transient creep in olivine rocks, *Tectonophysics*,
 685 279, 93–111, doi:10.1016/S0040-1951(97)00134-0.
- 686 Crittenden, M. (1967), Viscosity and Finite Strength of the Mantle as Determined from
 687 Water and Ice Loads*, *Geophysical Journal of the Royal Astronomical ...*, pp. 261–279,
 688 doi:10.1111/j.1365-246X.1967.tb06243.x.
- 689 Davis, J. L., B. P. Wernicke, and M. E. Tamisiea (2012), On seasonal signals in geode-
 690 tic time series, *Journal of Geophysical Research: Solid Earth*, 117(1), 1–10, doi:
 691 10.1029/2011JB008690.
- 692 Feigl, K. L., and W. Thatcher (2006), Geodetic observations of post-seismic transients in
 693 the context of the earthquake deformation cycle, *Comptes Rendus - Geoscience*, 338,
 694 1012–1028, doi:10.1016/j.crte.2006.06.006.
- 695 Fletcher, J. M., O. J. Teran, T. K. Rockwell, M. E. Osokin, K. W. Hudnut, K. J. Mueller,
 696 R. M. Spelz, S. O. Akciz, E. Masana, G. Faneros, E. J. Fielding, S. Leprince, A. E.
 697 Morelan, J. Stock, D. K. Lynch, A. J. Elliott, P. Gold, J. Liu-Zeng, A. González-
 698 Ortega, A. Hinojosa-Corona, and J. González-García (2014), Assembly of a large
 699 earthquake from a complex fault system: Surface rupture kinematics of the 4 April
 700 2010 El Mayor-Cucapah (Mexico) Mw 7.2 earthquake, *Geosphere*, 10(4), 797–827,
 701 doi:10.1130/GES00933.1.
- 702 Freed, A. M., R. Bürgmann, E. Calais, J. Freymueller, and S. Hreinsdóttir (2006), Impli-
 703 cations of deformation following the 2002 Denali, Alaska, earthquake for postseismic
 704 relaxation processes and lithospheric rheology, *Journal of Geophysical Research: Solid
 705 Earth*, 111, 1–23, doi:10.1029/2005JB003894.
- 706 Freed, A. M., R. Bürgmann, and T. Herring (2007), Far-reaching transient motions after
 707 Mojave earthquakes require broad mantle flow beneath a strong crust, *Geophysical
 708 Research Letters*, 34, 1–5, doi:10.1029/2007GL030959.
- 709 Gonzalez-Ortega, A., Y. Fialko, D. Sandwell, F. A. Nava-pichardo, J. Fletcher,
 710 J. Gonzalez-garcia, B. Lipovsky, M. Floyd, and G. Funning (2014), El Mayor-
 711 Cucapah (Mw7.2) earthquake: early near-field postseismic deformation from In-
 712 Sar and GPS observations, *Journal of Geophysical Research*, 119, 1482–1497, doi:
 713 10.1002/2013JB010193.Received.
- 714 Hauksson, E., J. Stock, K. Hutton, W. Yang, J. A. Vidal-Villegas, and H. Kanamori
 715 (2011), The 2010 Mw 7.2 El mayor-cucapah earthquake sequence, Baja Califor-
 716 nia, Mexico and Southernmost California, USA: Active seismotectonics along the
 717 Mexican pacific margin, *Pure and Applied Geophysics*, 168(3918), 1255–1277, doi:
 718 10.1007/s00024-010-0209-7.
- 719 Hearn, E. H. (2003), What can GPS data tell us about the dynamics of post-seismic defor-
 720 mation ?, (2003), 753–777.
- 721 Hearn, E. H., S. McClusky, S. Ergintav, and R. E. Reilinger (2009), Izmit earthquake post-
 722 seismic deformation and dynamics of the North Anatolian Fault Zone, *Journal of Geo-
 723 physical Research: Solid Earth*, 114(August 2008), 1–21, doi:10.1029/2008JB006026.

- Hetland, E. A. (2003), Postseismic relaxation across the Central Nevada Seismic Belt, *Journal of Geophysical Research*, 108(Figure 2), 1–13, doi:10.1029/2002JB002257.
- Hetland, E. A., and G. Zhang (2014), Effect of shear zones on post-seismic deformation with application to the 1997 Mw 7.6 manyi earthquake, *Geophysical Journal International*, 198, 259–269, doi:10.1093/gji/ggu127.
- Hines, T. T., and E. A. Hetland (2013), Bias in estimates of lithosphere viscosity from interseismic deformation, *Geophysical Research Letters*, 40(16), 4260–4265, doi:10.1002/grl.50839.
- Hines, T. T., and E. A. Hetland (2016), Rapid and simultaneous estimation of fault slip and heterogeneous lithospheric viscosity from post-seismic deformation, *Geophysical Journal International*, 204(1), 569–582, doi:10.1093/gji/ggv477.
- Jacobs, A., D. Sandwell, Y. Fialko, and L. Sichoux (2002), The 1999 (Mw7.1) Hector Mine, California, Earthquake: Near-Field Postseismic Deformation from ERS Interferometry, *Bulletin of the Seismological Society of America*, 92(May), 1433–1442.
- Johnson, K. M., and P. Segall (2004), Viscoelastic earthquake cycle models with deep stress-driven creep along the San Andreas fault system, *Journal of Geophysical Research: Solid Earth*, 109, 1–19, doi:10.1029/2004JB003096.
- Johnson, K. M., R. Bürgmann, and J. T. Freymueller (2009), Coupled afterslip and viscoelastic flow following the 2002 Denali Fault, Alaska earthquake, *Geophysical Journal International*, 176(3), 670–682, doi:10.1111/j.1365-246X.2008.04029.x.
- Jónsson, S., P. Segall, R. Pedersen, and G. Bjornsson (2003), Post-earthquake ground movements correlated to pore-pressure transients, *Nature*, 424(July), 179–183, doi:10.1038/nature01758.1.
- Kaufmann, G., and F. Amelung (2000), Reservoir-induced deformation and continental rheology in vicinity of Lake Mead, Nevada, *Journal of Geophysical Research*, 105(B7), 16,341, doi:10.1029/2000JB900079.
- Kroll, K. A., E. S. Cochran, K. B. Richards-Dinger, and D. F. Sumy (2013), Aftershocks of the 2010 Mw 7.2 El Mayor-Cucapah earthquake reveal complex faulting in the Yuha Desert, California, *Journal of Geophysical Research: Solid Earth*, 118(October), 6146–6164, doi:10.1002/2013JB010529.
- Lekic, V., S. W. French, and K. M. Fischer (2011), Lithospheric Thinning Beneath Rifted Regions of Southern California, *Science*, 334(November), 783–787.
- Liu, H.-P., D. L. Anderson, and H. Kanamori (1976), Velocity dispersion due to anelasticity; implications for seismology and mantle composition, *Geophysical Journal International*, 47(1), 41–58, doi:10.1111/j.1365-246X.1976.tb01261.x.
- Lundgren, P., E. A. Hetland, Z. Liu, and E. J. Fielding (2009), Southern San Andreas-San Jacinto fault system slip rates estimated from earthquake cycle models constrained by GPS and interferometric synthetic aperture radar observations, *Journal of Geophysical Research: Solid Earth*, 114(2), 1–18, doi:10.1029/2008JB005996.
- McGuire, J. J., and P. Segall (2003), Imaging of aseismic fault slip transients recorded by dense geodetic networks, *Geophysical Journal International*, 155(3), 778–788, doi:10.1111/j.1365-246X.2003.02022.x.
- Meade, B. J., and B. H. Hager (2005), Block models of crustal motion in southern California constrained by GPS measurements, *Journal of Geophysical Research B: Solid Earth*, 110, 1–19, doi:10.1029/2004JB003209.
- Murray, J. R., and P. Segall (2005), Spatiotemporal evolution of a transient slip event on the San Andreas fault near Parkfield, California, *Journal of Geophysical Research : Solid Earth*, 110(9), 1–12, doi:10.1029/2005JB003651.
- Nur, A., and G. Mavko (1974), Postseismic viscoelastic rebound, *Science*, 183(4121), 204–206, doi:10.1038/098448b0.
- O'Connell, R. J. (1971), Rheology of the Mantle, *EOS, Transactions, American Geophysical Union*, 52, 140–142.
- Oskin, M. E., J. R. Arrowsmith, A. Hinojosa Corona, A. J. Elliott, J. M. Fletcher, E. J. Fielding, P. O. Gold, J. J. Gonzalez Garcia, K. W. Hudnut, J. Liu-Zeng, and O. J. Teran

- 778 (2012), Near-field deformation from the El Mayor-Cucapah earthquake revealed by
 779 differential LIDAR, *Science*, 335(6069), 702–705, doi:10.1126/science.1213778.
- 780 Pollitz, F., C. Wicks, and W. Thatcher (2001), Mantle Flow Beneath a Continental Strike-
 781 Slip Fault : Postseismic Deformation After the 1999 Hector Mine Earthquake, *Science*,
 782 1814(2001), 1814–1818, doi:10.1126/science.1061361.
- 783 Pollitz, F. F. (2003), Transient rheology of the uppermost mantle beneath the Mo-
 784 jave Desert, California, *Earth and Planetary Science Letters*, 215, 89–104, doi:
 785 10.1016/S0012-821X(03)00432-1.
- 786 Pollitz, F. F., G. Peltzer, and R. Bürgmann (2000), Mobility of continental mantle: Evi-
 787 dence from postseismic geodetic observations following the 1992 Landers earthquake,
 788 *Journal of Geophysical Research*, 105(1999), 8035, doi:10.1029/1999JB900380.
- 789 Pollitz, F. F., R. Bürgmann, and W. Thatcher (2012), Illumination of rheological mantle
 790 heterogeneity by the M7.2 2010 El Mayor-Cucapah earthquake, *Geochemistry, Geo-
 791 physics, Geosystems*, 13(6), 1–17, doi:10.1029/2012GC004139.
- 792 Pollitz, F. F. (2015), Postearthquake relaxation evidence for laterally variable viscoelastic
 793 structure and water content in the Southern California mantle, *Journal of Geophysical
 794 Research: Solid Earth*, 120, 2672–2696, doi:10.1002/2014JB011603.
- 795 Rauch, H. E., F. Tung, and C. T. Striebel (1965), Maximum likelihood estimates of linear
 796 dynamic systems, *AIAA Journal*, 3(8), 1445–1450.
- 797 Riva, R. E. M., and R. Govers (2009), Relating viscosities from postseismic relaxation to
 798 a realistic viscosity structure for the lithosphere, *Geophysical Journal International*, 176,
 799 614–624, doi:10.1111/j.1365-246X.2008.04004.x.
- 800 Rollins, C., S. Barbot, and J.-P. Avouac (2015), Postseismic Deformation Following the
 801 2010 M7.2 El Mayor-Cucapah Earthquake : Observations , Kinematic Inversions , and
 802 Dynamic Models, *Pure and Applied Geophysics*, doi:10.1007/s00024-014-1005-6.
- 803 Savage, J. C. (1990), Equivalent strike-slip earthquake cycles in half-space and
 804 lithosphere-asthenosphere earth models, *Journal of Geophysical Research*, 95, 4873,
 805 doi:10.1029/JB095iB04p04873.
- 806 Savage, J. C., and J. L. Svart (2009), Postseismic relaxation following the 1992 M 7.3
 807 Landers and 1999 M 7.1 Hector Mine earthquakes , southern California, *Journal of
 808 Geophysical Research*, 114(B01401), doi:10.1029/2008JB005938.
- 809 Savage, J. C., J. L. Svart, and S. B. Yu (2005), Postseismic relaxation and transient creep,
 810 *Journal of Geophysical Research: Solid Earth*, 110, 1–14, doi:10.1029/2005JB003687.
- 811 Segall, P., and M. Mathews (1997), Time dependent inversion of geodetic data, *Journal of
 812 Geophysical Research*, 102.
- 813 Spinler, J. C., R. A. Bennett, C. Walls, L. Shawn, and J. J. G. Garcia (2015), As-
 814 sessing long-term postseismic deformation following the M7.2 4 April 2010, El
 815 Mayor-Cucapah earthquake with implications for lithospheric rheology in the
 816 Salton Trough, *Journal of Geophysical Research: Solid Earth*, 120, 3664–3679, doi:
 817 10.1002/2014JB011613.Received.
- 818 Wei, M., D. Sandwell, Y. Fialko, and R. Bilham (2011a), Slip on faults in the Imperial
 819 Valley triggered by the 4 April 2010 Mw 7.2 El Mayor-Cucapah earthquake revealed by
 820 InSAR, *Geophysical Research Letters*, 38(January), 1–6, doi:10.1029/2010GL045235.
- 821 Wei, M., Y. Liu, Y. Kaneko, J. J. McGuire, and R. Bilham (2015), Dynamic triggering of
 822 creep events in the Salton Trough, Southern California by regional M5.4 earthquakes
 823 constrained by geodetic observations and numerical simulations, *Earth and Planetary
 824 Science Letters*, 427, 1–10, doi:10.1016/j.epsl.2015.06.044.
- 825 Wei, S., E. Fielding, S. Leprince, A. Sladen, J.-P. Avouac, D. Helmberger, E. Hauksson,
 826 R. Chu, M. Simons, K. Hudnut, T. Herring, and R. Briggs (2011b), Superficial sim-
 827 plicity of the 2010 El MayorCucapah earthquake of Baja California in Mexico, *Nature
 828 Geoscience*, 4(9), 615–618, doi:10.1038/ngeo1213.
- 829 Yang M., and M. N. Toksöz (1981), Time-dependent deformation and stress relaxation
 830 after strike-slip earthquakes, *Journal of Geophysical Research*, 86, 2889–2901.

- 831 Yuen, D. A., and W. R. Peltier (1982), Normal modes of the viscoelastic earth, *Geo-*
832 *physical Journal of the Royal Astronomical Society*, 69, 495–526, doi:10.1111/j.1365-
833 246X.1982.tb04962.x.